

On a layer model for spilling breakers: a preliminary experimental analysis.

A. Lucarelli^{a,b}, C. Lugni^{a,c}, M. Falchi^a, M. Felli^a, M. Brocchini^b

^a*CNR-INSEAN, Rome, Italy*

^b*Univ. Politecnica delle Marche, Ancona, Italy*

^c*AMOS, NTNU, Trondheim, Norway*

Abstract

Accurate and reliable experimental data of a sloshing-induced, rapidly-evolving spilling breaker, are used to understand the specific physics of this phenomenon and to partially evaluate a simplified analytical model by Brocchini and co-workers. Such a model is based on a three-layer structure: an underlying potential flow, a thin, turbulent single-phase layer in the middle and a turbulent two-phase layer (air-water) on the upper part. The experiments were carried out by using a 3m long, 0.6m deep and 0.10m wide tank, built in Plexiglas and forced through an hexapode system, this allowing for an high accuracy of the motion. Mean and turbulent kinematic quantities were measured using the Particle Image Velocimetry (PIV) technique. To ensure repeatability of the phenomenon, a suitable breaker event was generated to occur during the first two oscillation cycles of the tank. The tank motion was suitably designed using a potential (HPC) and a Navier-Stokes solver. The latter, was useful to understand the dimension of the area of interest for the measurements. The evolution of the breaker is described in terms of both global and local properties. Wave height and steepness show that after an initial growth, the height immediately decays after peaking, while the wave steepness remains constant around 0.25. The evolution of the local properties, like vorticity and turbulence, vortical and turbulent flows displays the most interesting dynamics. Two main stages characterise such evolution. In stage (1), regarded as a “build-up” stage, vorticity and TKE rapidly reach their maximum intensity and longitudinal extension.

During such stage the thickness of the single-phase turbulent region remains almost constant. Stage (2), is regarded as a “relaxation” stage, characterised by some significant flow pulsation till the wave attains a quasi-steady shape. In support to the analytical, three-layer model of Brocchini and co-workers it is demonstrated that the cross-flow profile of the mean streamwise velocity U inside the single-phase turbulent layer is well represented by a cubic polynomial. However, differently from available steady-state models the coefficient of the leading-order term is function of time: $A = A(s, t)$. During stage (1) a fairly streamwise-uniform distribution of U is characterized by $A(s, t) \approx 1$, while during stage (2) U is less uniform and A varies over a much larger range.

Keywords: spilling breaker, turbulent region, PIV experiments, flow unsteadiness

1. Introduction

Wave breaking plays a fundamental role in marine dynamics, evolving at the most varied scales: from the global heat and mass transfer occurring at the air-sea interface (e.g. [1];[2]; [3]), to the dissipation of wave energy and momentum (e.g. [4]; [5]; [6]), to the more local dynamics like the erosion of beaches (e.g. [7]; [8]), the transport of seabed sediments and the interaction with ships and structures (e.g. [9]; [10]).

Also because of such ubiquity, wave breaking displays a number of modalities and characteristics (e.g. [11]; [12]), all leading to turbulent dissipative processes (e.g. [5]; [13]; [14]). Hence, the study of breaking waves represents a major challenge for scientists and researchers. In this respect we here limit our attention to the specific class of spilling breakers, though we believe that some of the analysis also applies to plungers.

Most of the analysis available on spilling breakers refers to quasi-steady breakers. Peregrine [15] suggests a criterion to distinguish between quasi-steady and unsteady spilling breakers: a spiller is taken as quasi-steady (in a frame of reference moving with the wave) if its deformation evolves at longer time scales

than those typical of the motion of water through the turbulent region. The structure of such quasi-steady breakers is that of an initial mixing layer region, generated at the leading edge (toe) by shear stresses due to the relative motion between the turbulent wave surface and the water in which the wave propagates, followed by a region beneath the crest of the wave where gravity influences and restrains the turbulent motions near the surface ([16]; [17]).

More recently the focus is shifting to the description of unsteady spillers [11], characterized by rapid and intense deformation (e.g. significant curvature) and rotation of the near-surface turbulent region. The conceptual model for such rapidly-evolving spillers (among which also the “whitecaps”), i.e. analogy with mixing layers followed by wakes, is similar to those of quasi-steady spillers but it differs in the description of the near-surface two-phase flow dynamics ([18]; [19] [20]; [21]) and turbulent-mean flow relations [22]. In brief the model proposed by Brocchini and co-workers is composed of three layers (see Fig. 1): a top two-phase flow layer where air and water mix; a middle, single-phase turbulent layer and the wave body, thought of being irrotational. A similar, though less physically-comprehensive, approach has been recently used to study Favre waves and the shoaling and breaking of solitary waves [23].

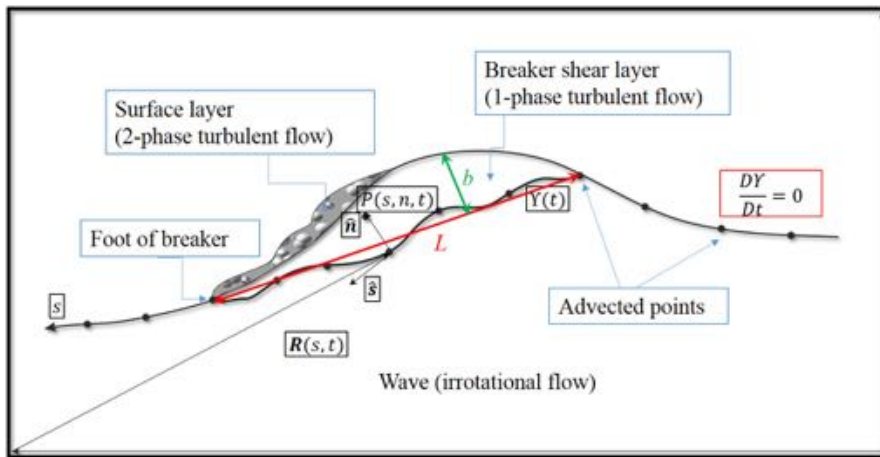


Figure 1: Schematic view of the theoretical model of Brocchini [18].

The present contribution is part of a comprehensive and detailed study aimed

at: 1) investigating the overall and specific near-surface dynamics of a rapidly-evolving spilling breaker, 2) supporting and validating the analytical model by Brocchini and co-workers. The study is based on accurate laboratory experiments, whose preliminary results are reported in this paper.

The next section illustrates how the laboratory experiments have been designed and carried out, while section 3 summarizes the main results concerning both geometry and internal wave kinematics. A final section proposes a discussion of the same results and closes the paper.

2. Laboratory experiments

In most of previous experimental studies, a spilling breaker was analysed in similarity with either hydraulic jumps [24] or hydrofoil-generated turbulence [25], such flows being quasi-steady, characterized by a weakly curved free surface and almost vanishing local rotation.

Being the aim of this work that of studying, with a very high spatial resolution and good repeatability, a rapidly-evolving spilling breaker, we have decided to resort to an impulsive generation of the breaker (see Fig. 2, right panel). Furthermore, the choice of a sloshing tank allows for a high repeatability of the phenomenon and a good accuracy of measurement.

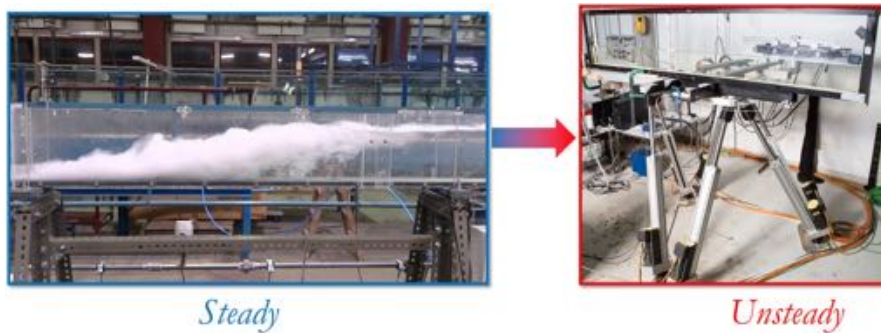


Figure 2: Left panel: a flume for the generation of a hydraulic jump. Right panel: Hexapode System for the generation of an unsteady spilling breaker.

2.1. Design of the experiments

The experiments were conducted at the Sloshing Laboratory of the CNR-INSEAN (Marine Technology Research Institute), Rome, Italy.

The spilling breaker was reproduced into a 3 m long, 0.6 m deep and 0.1 m wide tank made of Plexiglas. A Symetrie Mistral Hexapode system was used to force the motion of the tank and ensured a high accuracy of the motion with a resolution of the order of 0.1 mm (see Fig. 2, right panel).

The design of the experiments at hand required the tackling of several challenges, first, a reliable measurement of the turbulent flow field, which characterizes the breaker in the region surrounding the wave crest, requires a statistical analysis, i.e. a large number of independent events, each given by one single run. The capability to generate a spilling breaker with high repeatability becomes, then, a crucial issue for the reliability of the statistical analysis. In similarity to previous studies on the evolution of breaking waves induced by shallow sloshing flows (e.g. [26], [27]), a suitable spilling breaker was designed to evolve in a sloshing tank by means of a combination of numerical solutions.

An efficient HPC solver [28], for the solution of a potential flow was first used to reproduce the flow evolving in a 3 m long, 0.6 m deep and 0.1 m wide tank with still water depth $h_0 = 0.2$ m, where the temporal evolution of the free surface was evaluated in terms of fully Lagrangian, nonlinear kinematic and dynamic boundary conditions. This specific type of runs allowed us to estimate the time history of the motion, velocity and acceleration of the tank. To avoid vibrations and mechanical noise, the motion was generated as smoothly as possible, at least during the acquisition of the kinematic flow field. The overall forcing motion is shown in Fig. 3. We can distinguish a first interval (“forcing stage”) for $0s \leq t \leq 1.195s$, denoted by the red dashed line. In the following instants, $1.195s < t \leq 4.0708s$, a suitable time history was created to bring the tank in position, with no sudden decelerations (“decay stage”, $1.95s \leq t \leq 2.50s$ and “to-rest stage”, $2.50s \leq t \leq 4.07s$).

The equations that represent the path, velocity and acceleration of the tank,

are, respectively:

$$x(t) = A(1 - \cos(\omega t)) - 0.335(t - t_1) + 0.084 - 0.335 \sin(t - t_2) - 0.353 \quad (1)$$

$$v(t) = \omega A(\sin(\omega t)) - 0.335 - 0.335 \cos(t - t_2) \quad (2)$$

$$a(t) = \omega^2 A(\cos(\omega t)) + 0.335 \sin(t - t_2) \quad (3)$$

where $A = 0.075m$ (oscillation amplitude), $\omega = 3.9517rad/s$ (angular frequency), $t_1 = 1.95s$, $t_2 = 2.5s$, $t_{end} = 4.07s$. The values of displacement (R_x and R_y), velocity (v) and acceleration (a) achieved with the above-mentioned equations, must fall within the motion limits of the Hexapode system, which are: $R_x = \pm 0.47m$, $R_y = \pm 0.47m$, $v = 1m/s$, $a = 10m/s^2$. Figure 3 shows that such limits were respected.

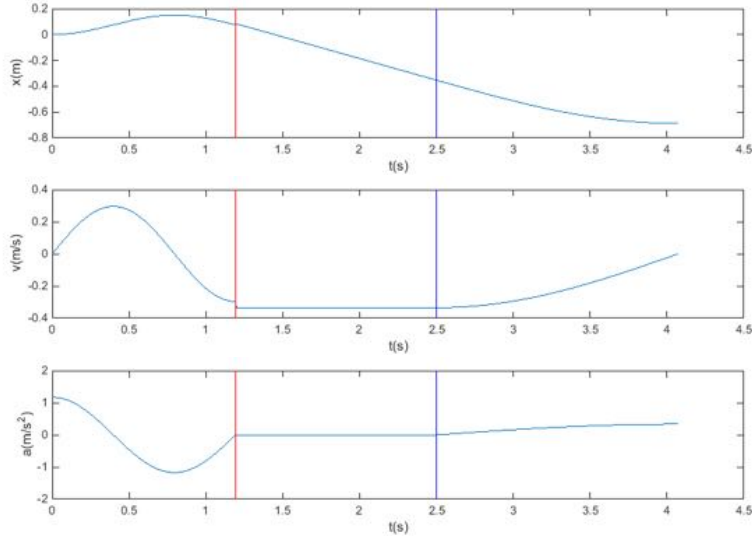


Figure 3: Time history of the motion (top panel), velocity (middle panel) and acceleration (bottom panel) of the tank.

One of the most important advantages of the HPC solver is the reduced computational time, which made it possible to test several different time histories till finding the most suited for our purpose. Care was put in the realization of the breaking event during the first oscillation of the tank. According to Lugni et al. ([27], [29], [30], [31]) the technique in use allows for a high repeatability of

the sloshing flows, where large nonlinear local effects can make the event highly chaotic in the successive cycles.

Further, the capability to control the flow features during the first oscillation (mainly governed by the initial conditions) enables the realization of an unsteady, strongly nonlinear breaking event, i.e. close to the sought physical breaker. Figure 4 (left panel) shows that the HPC solver allows to follow the wave generation and the wave steepening up to the onset of breaking. The following stages cannot be reproduced with the HPC solver because it cannot resolve the evolution of vortical and turbulent flows, but only a potential flow.

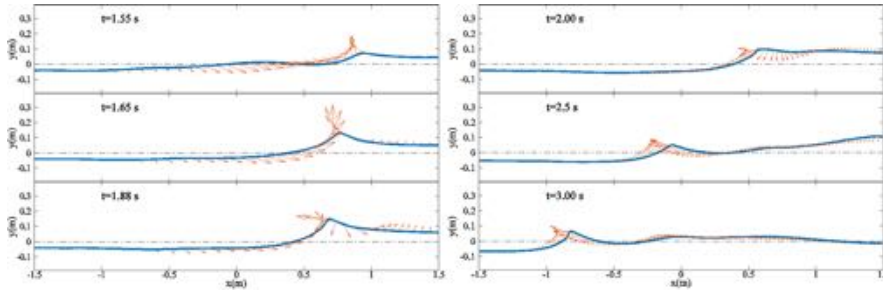


Figure 4: Evolution of the free surface before (left column: HPC solver) and after the breaker generation (right column: NS solver).

For this reason, in order to assess and follow the complete evolution of the spilling breaker, with the aim to optimize the arrangement of the PIV setup (cameras + laser source, see the top panel of Fig. 6) necessary for the measurement of the kinematic field, the time history found with the HPC solver, was also inspected through a Navier-Stokes (NS) solver [32]. In particular, the NS solver (see the right column of Fig. 4) was useful to estimate the size of the region where the breaker would initiate and evolve, this region having a length of about 1.80 m and a height variable according to the evolution of the breaker, but with a maximum extension of about 0.35 m. The large extent of the region of interest and the need to undertake detailed flow measurements with a good spatial resolution, suitable to accurately resolve the evolution of the turbulent flow structures in the spilling breaker, required the implementation of an ad-hoc camera arrangement and acquisition strategies.

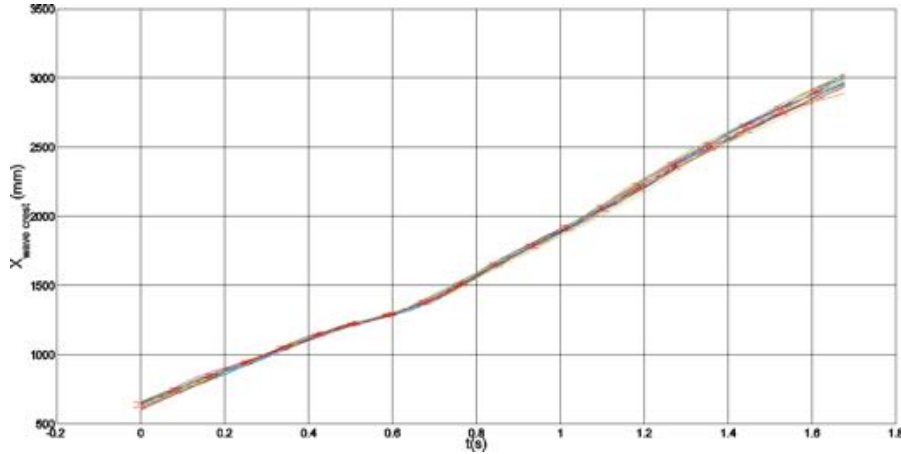


Figure 5: Horizontal position of the wave crest (mm).

2.2. Repeatability analysis

The repeatability analysis is essential to verify the accuracy of the present experimental study.

The tank motion designed by the HPC solver, was used in the laboratory to reproduce the phenomenon. The repeatability of the global features was first assessed through the analysis of the recorded images, with particular attention to some geometrical parameters: horizontal position of the wave crest, horizontal position of the breaker toe and horizontal position of the tank.

The main reference geometrical point was the wave crest horizontal position. More in detail, a set of 32 runs of the same event were investigated. This was performed using a simplified configuration with two digital cameras (frame rate = 100 fps and resolution 1920×1088) and diffused light. The repeatability analysis, based on the horizontal position of the wave crest, provides an error estimate within 10mm, which is of the same order of the camera resolution. Figure 5 shows the plot of the horizontal position of the wave crest versus time. The small size of the errorbars (red line and circles), confirms the high repeatability of the phenomenon and, therefore, the possibility to proceed to the definition of the experimental setup.

2.3. Experimental setup

A 2D Particle Image Velocimetry (PIV) technique was used for the measurement of the instantaneous velocity field. The still water depth was $h_0 = 0.20$ m.

The large extension of the region of interest, suggested to divide this area into two different zones, in order to reach a good spatial and temporal resolution as shown in Fig. 6 (bottom). For each zone a multi-camera simultaneous recording system with 4 cameras arranged side by side was used to acquire a large flow extent at a spatial resolution, adequate to resolve flow eddies as small as 2mm. With this arrangement, the field of view of the camera system allowed us to cover about half of the region of interest and, thus, created the need to split it in two regions. Namely:

- an upstream region, indicated with the black rectangles in the bottom panel of Fig. 6, which covers the formation and evolution of the breaker until a quasi-steady is reached. As a consequence, the evolution of the wave profile required to arrange the cameras at different vertical positions. This was achieved inclining the cameras by 7 deg in the vertical plane (see image A of Fig. 6).
- a downstream region, indicated by the red rectangles in the bottom panel of figure 6, which covers the rest of the breaker evolution.

The 4 cameras used for the PIV image recording were Imager sCMOS models by LaVision (i.e. 16 bits, 2560×2160 pixel resolution, $6.5 \mu\text{m}$ pixel size, 50 frames/s maximum frame rate). Each camera was equipped with a 50 mm lens and positioned at the distance of 800 mm from the laser sheet. It gave a magnification factor of about 9 pix/mm. This means that each pixel in the image is about 0.11mm^2 in the physical scale and allows to evaluate the relative overlapping between two subsequent Fields of View of the cameras.

The water was seeded with hollow glass particles of mean diameter of about $10 \mu\text{m}$, well suited for flows with characteristic velocities in the order of few

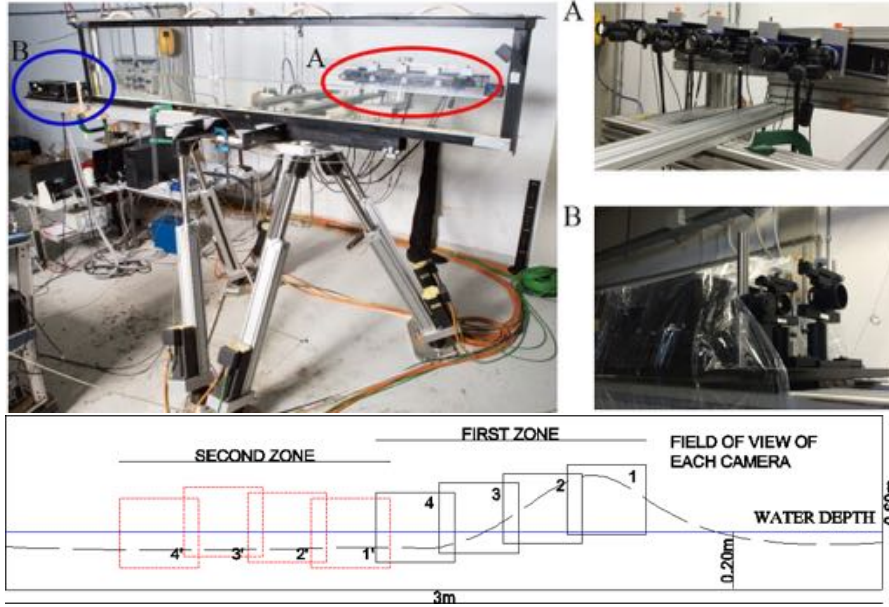


Figure 6: Experimental set-up: Exapode System, tank, laser and cameras (top-left panel); cameras in the upstream region inclined by 7 deg in the vertical plane (top-right panel, image A) and laser with cylindrical and spherical lenses (top-right panel, image B); region of interest for the PIV measurements (bottom panel).

meters per second. They offer a good scattering efficiency and a sufficiently small velocity lag. Further, the chosen seeding particle diameter yields a particle diameter in the image of $d_{pi} = 0.09$ px. This is sufficient to resolve the particles.

The illumination was provided by a double cavity Nd-Yag laser (2×200 mJ/pulse @ 12.5 Hz by Quantel). The laser beam was expanded through a set of one cylindrical (i.e. -15 mm focal length) and one spherical (i.e. 1000 mm focal length) lenses to obtain an illumination domain extended over the whole region of interest and 1mm thick (see Fig. 6, image B).

A frame rate of 8 fps was the maximum value compatible between the laser source frequency and the camera frame rate. In order to increase the frame rate from 8 to 16 fps, the laser trigger was shifted by $1/2dt$, where dt was the sampling period of the PIV system. This implies that the PIV snapshots were recorded at instants $t_i = t_0 + idt$ during the first data collection and at

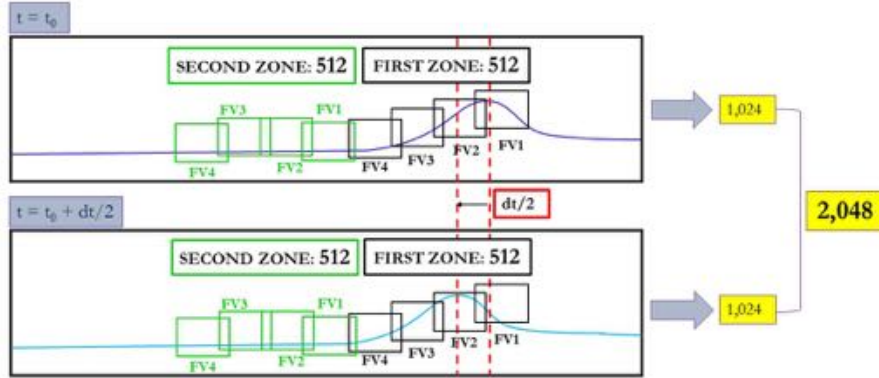


Figure 7: Schematic representation of the two different temporal configurations of cameras recording.

$t_i = t_0 + 0.5dt + idt$ during the second data collection, with $i = 1, \dots, T/dt$, and T indicating the total acquisition time. In particular, the sampling period dt was $1/8s$ and the acquisition time was $T = 1.5sec$. The value of dt was found by the simple relation: $\Delta x/v$ where v ($1.2m/s$) was the wave crest velocity evaluated by the NS solver simulation and Δx (10 pixel) were the pixel corresponding to 1 cm and calculated through the magnification factor. For each zone of each temporal configuration 512 realizations were run, for a total number of 1,024 realizations. Considering both temporal configurations, 2,048 realizations were run (see Fig. 7).

For the whole experimental campaign, the PIV images were processed by the La Vision software DaVIS 8.2, which uses a multi-pass cross-correlation image algorithm with windows deformation [33]. PIV images were pre-processed masking the image region over the water surface and subtracting the minimum background value. The final size of the interrogation windows was 24×24 pixels with an overlap of 75%.

The subimage within the interrogation window was then cross correlated with the corresponding subimage in the subsequent image. The position of the peak in the cross correlation result provides a measure of the displacement of the structure in the second subimage with respect to the first. In this way,

an accurate estimation of the instantaneous velocity field was achieved and the large number of repetitions has supported an accurate statistical analysis, which is very important for the characterization of the flow structure.

3. Results

The available dataset allows for useful insight both in the overall dynamics of the breaker and in the details of dynamics of the single-phase, turbulent layer of the model of [18]. Specific emphasis is put in highlighting the differences between dynamics of a steady breaker, like an hydraulic jump, and a rapidly-evolving breaker, like the breaker of interest here.

Hence, the following aspects are investigated in detail: i) the near-surface breaker topology, ii) the injection/generation of vorticity at the free surface, iii) the overall turbulent kinetic energy field and the detection of the single-phase turbulent region, iv) the geometry of the single-phase turbulent region.

Both the maps of each quantity of interest and the result of the mean of 512 realizations are superposed to the related underlying flow image. The data have been cropped with a numerical mask, in order to visually remove the effects of the three-dimensionality.

As mentioned in the previous section, we only focus on the first zone (see Fig. 7), where the flow is characterized by the highest curvature and rotation. These, clearly, highlighting the unsteadiness of the phenomenon, confirmed by Peregrine's criterion [15]: comparing the time needed for the crest deformation, about 0.65s, to the time needed for a particle to cross in the streamwise direction the single-phase turbulent region, about 0.75 s, we find the fairly rapid crest deformation typical of an unsteady breaker.

3.1. Overall evolution

The breaker has been generated through a sloshing flow because it is highly repeatable, very unsteady and allows for suitable resolution of the near-surface

flow. Repeatability is ensured by analyzing only the first wave event generated within the tank (e.g. [27], [29], [30], [31], [34]). Such high repeatability is essential for the following reasons:

- i) the flow evolution close to the air-water interface can be properly studied by means of a statistical approach (ensemble averaging), which enables a reliable interpretation of the turbulent flow at the interface;
- ii) the measured dataset is certified for validation and verification of numerical solvers.

Fig. 8 shows the global scenario during the generation and evolution of the event. The time increases from top to bottom and from left to right. The top left image corresponds to $t = 1.64$ s, the bottom right image to $t = 2$ s, with $t = 0$ identifying the start of the tank motion ($t = 0$); a time step $\Delta t = 0.04$ s exists between two consecutive images. All the sequence evolves during the “decay stage” described in the previous section. During the first 4 instants (left column of Fig. 8), the tank moves leftward with constant speed and zero acceleration (linear motion, see Fig. 3). The wave moves in the same direction of the tank and becomes asymmetric with respect to the vertical axis which passes through the crest (indicated by the left dashed line in the figure). Such asymmetry is initiated by the tank motion, i.e. the right wall pushes the water (first two images), and then emphasized by the crest slowdown [35] which causes the steepening of the wave crest. Because of the unsteadiness of the phenomenon, the wave changes quickly its shape leading to a breaker here roughly identified by some air trapping in the wave front (see the air-water mixture starting at $t = 1.72$ s). This is the easiest criteria to visually identify the occurrence of a breaker from global images of the phenomenon.

Although at this stage we refer just to a sequence of images, i.e. no local geometrical measurements are given, we can qualitatively observe that the local curvature at the crest increases until $t = 1.8$ s (see the bottom panel of the left column in Fig. 8) and, then, progressively decreases to reach an almost steady value at $t = 1.92$ s (see the third panel of the right column of figure 8).

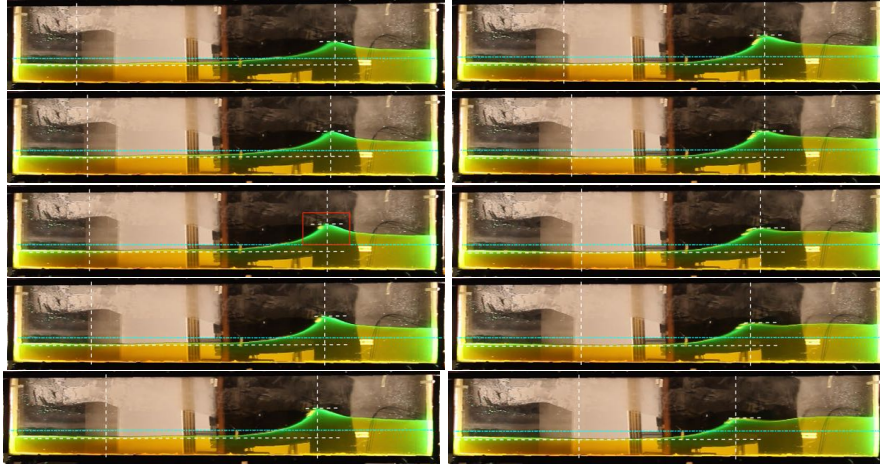


Figure 8: Image sequence of the generation and evolution of the spilling breaker in the sloshing tank. The time increases from top to bottom and from left to right with an initial time 1.64 s, final time 2.0 s and time step of $1/25$ s.

Portability of the results has been achieved by making them dimensionless. The most suited scales (length and time) for such an operation are, obviously, function of the specific flow at hand.

The literature on sloshing flows (e.g. [36], [37], [38]) suggests as suitable scales the filling water depth h_0 and the natural period of the tank T_0 (here 4.3s). In particular, for shallow-water condition, i.e. for $h_0/\lambda \leq 0.1$, where λ is the wavelength, an unsteady breaker evolving to a steady breaker is commonly identified for $T/T_0 \simeq 1$ [37]. In the present case, the motion of the tank is not explicitly excited at a frequency close to $1/T_0$; then we cannot a priori assess that the breaker is in shallow-water condition.

To better understand the flow conditions governing the evolution of the prescribed event, Fig. 9 shows the time history of the wave steepness ($kH/2$), wave height (H) and wavelength measured from the images shown in Fig. 8.

Fig. 10 shows geometrical quantities of interest, as well as the comparison with the free-surface configuration achieved from the numerical solver used to design the experiment.

The wavelength is estimated as twice the horizontal distance between the

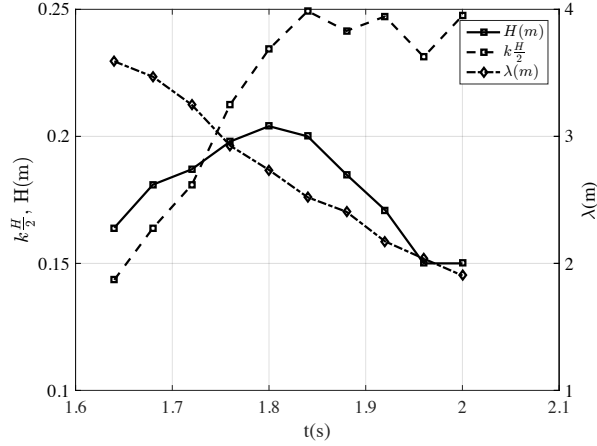


Figure 9: Evolution of the wave steepness, wave height and wavelength in time where $t_1 = 1.64$ s is the time of the first inspected image with respect to the starting of the tank motion.

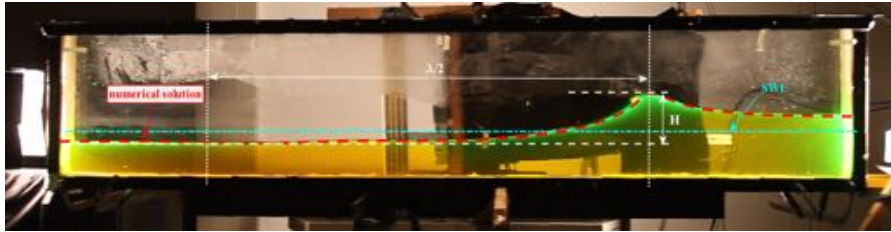


Figure 10: Definition of the geometrical quantities measured from the image analysis. Red dashed line represents the free-surface configuration calculated through the numerical solver used in the design of the experimental tank motion.

maximum and minimum elevation of the free surface (see the vertical, white dashed lines in Fig. 10). The wave height is the vertical distance between the same points (see the horizontal, white dashed lines in Fig. 10).

According to the above observations, Fig. 9 confirms the growth of the wave height until $t = t_1 + 0.16 = 1.8$, then its decay. Conversely, the wavelength decreases almost linearly; this behaviour causes an increase of the wave steepness until $t = 1.84$; then it keeps constant around a value $0.23 - 0.25$. The wavelength varying between 2 and 3.6 m, i.e. $h_0/\lambda < 0.1$, indicates that the flow evolves in shallow-water conditions.

This is further confirmed by the instantaneous period dominating the flow,

shown in Fig. 11, and calculated through a wavelet analysis of the wave elevation at 5 cm from the right (left panel) and left wall (right panel) of the tank, respectively. First (dash-dotted line), second (dotted line) and third (dashed line) natural sloshing periods are also indicated.

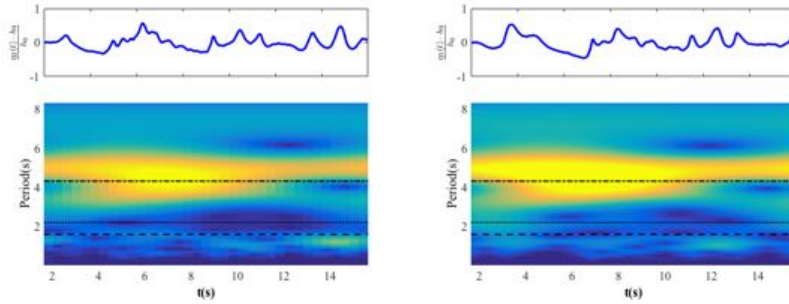


Figure 11: Time evolution of the wave elevation (blue lines) and corresponding wavelet analysis at two probes placed at 5 cm from the right wall (left panel), and at 5 cm from the left wall (right panel) of the tank, respectively.

The wave period that governs the flow evolution is almost equal to the largest natural period T_0 of the tank. This means that the corresponding wavelength is twice the length of the tank, i.e. $h_0/\lambda < 0.1$. However, to definitely assess the occurrence of shallow-water conditions, the empty circles in Fig. 12 show the ratio H/h_0 as function of λ/h_0 during the experimental evolution of the breaker from $t = 1.64$ to $t = 2$. Several limiting curves taken from the literature are also reported. The continuous line represents the limiting curve for the validity of the cnoidal wave theory, i.e. $Ur = H\lambda^2/h_0^3 > 40$, while for lower values the Stokes theory should be used. The dash-dotted line indicates the highest waves determined by computational studies according to the results of Williams [39]. The dotted line bounds the deep-water breaking limit, while the dashed line gives the corresponding limit in shallow waters. The present experimental data are, at least after the onset of breaking, larger than the shallow-water wave breaking limit, and in any case, larger than the shallow-water limit $\lambda/h_0 = 10$. Then, shallow-water conditions can be definitely assumed, which implies that the still-water level h_0 can be taken as suitable reference length scale. The scale

for the time comes from $T = \sqrt{h_0/g}$, g giving gravity acceleration, therefore in the following the dimensionless time $t^* = t\sqrt{g/h_0}$ is used.

At this point we are able to make dimensionless the evolution of the wave height and wavelength. This is shown in Fig. 13, where starred symbols give dimensionless variables.

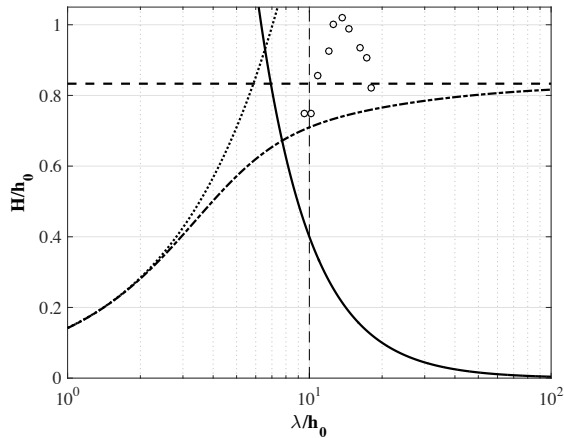


Figure 12: Literature limiting curves and our experimental data (empty circles).

We also analysed the possible influence of capillary waves on the onset of the breaker and on its successive evolution. Although observation of the images does not reveal any capillary wave at the forward face of the crest, a more quantitative analysis has been performed to demonstrate that capillaries are actually negligible for this flow. We, thus, refer to the radius of curvature of the crest region, which is large enough that surface tension effects are negligible and do not influence the breaking process. The data illustrated in Fig. 9 enable an estimation of the Bond number (Bo), which measures the importance of surface tension with respect to buoyancy effects:

$$Bo = \frac{\Delta\rho g}{\gamma k^2}$$

where $\Delta\rho$ is the density difference between water and air, γ the water surface tension and k the wave number.

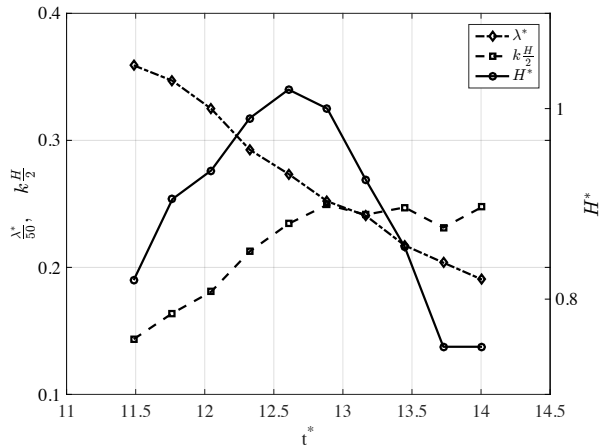


Figure 13: Dimensionless time evolution of the wave steepness, wave height and wavelength. The latter one is scaled by a factor 50.

Moreover, table 1 summarises the main geometric characteristics of the wave in both dimensional and dimensionless form.

The measured wavelengths are much larger than the typical wavelength of capillary waves, that is $\mathcal{O}(\infty)$ cm; the same is true for the Bond number ($Bo \gg 100$). These two parameters confirm that surface tension does not influence the breaking process investigated.

Fig. 14 summarises the results of some DNS numerical computations used to characterize the breaking regimes and the possible influence of the capillary waves [40]. In such figure, some of the experimental results existing in literature, summarized in the table of Fig. 15, are also reported. The symbols represent literature experimental data, the lines indicate the boundaries of the wave breaking regimes identified through the DNS simulations by [40]. Such regimes are denoted as follows: i) *PB*, which represents the plunging regime; ii) *SB*, which gives the spilling regime; iii) *PCW*, which indicates the presence of parasitic capillary waves and iv) *NB*, which gives the non-breaking gravity wave regime. The red line is the limiting curve between plunging and spilling breakers. The horizontal solid line (black line), coincident with the critical steepness $kH/2 = 0.32$ line, is the boundary between non breaking and plunging breakers.

$t(\text{image})$	$H(m)$	$\lambda(m)$	$kH/2$	Bo	t^*	H^*	λ^*
1.64 s	0.1646	3.6013	0.1435	44137	11.486	0.823	18.0065
1.68 s	0.1812	3.4724	0.1639	41035	11.766	0.906	17.362
1.72 s	0.1870	3.2621	0.18	36215	12.046	0.935	16.310
1.76 s	0.1979	2.923	0.2126	29078	12.326	0.989	14.615
1.80 s	0.2042	2.7362	0.2343	25480	12.606	1.021	13.681
1.84 s	0.2000	2.512	0.25	21475	12.886	1.000	12.56
1.88 s	0.1854	2.4108	0.2415	19780	13.167	0.927	12.054
1.92 s	0.1708	2.1699	0.2472	16025	13.447	0.854	10.849
1.96 s	0.1500	2.0363	0.2313	14112	13.727	0.750	10.181
2.00 s	0.1500	1.903	0.2475	12325	14.007	0.750	9.515

Table 1: Temporal evolution of the main geometrical characteristics of the wave in dimensional and dimensionless form.

It is also coincident with the numerical occurrence of spilling breaker, i.e. it is an extension of the red line. The black dashed line bounds the region between spilling and parasitic capillary waves. Finally, the dot-dashed line at $Bo = 67$, gives the critical Bond number for the appearance of parasitic capillaries. The filled circles around $kH/2 = 0.32$, even for the NB regime suggest literature experimental data with occurrence of spilling breakers generated with different physical mechanisms. This is in reasonable agreement with our data: breaking evolution occurs for a steepness ranging from 0.18 to 0.25 and a Bond number around or larger than 10^4 . Results very similar were achieved by Tulin & Waseda [41] (see stars in Fig. 14).

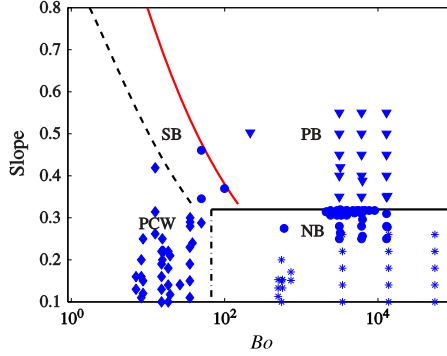


Figure 14: Wave state diagram, compares the regimes obtained through the simulation. (Adapted from [40]).

Reference	Wave type	λ (m)	Bo	Slope (ak)	Re	Generation	Measurement
Rapp & Melville (1990)	Plunger	1–2	3000–12 000	0.35–0.55	$3–9 \times 10^6$	Wave maker	Camera & wave gauges
—	Spiller	1–2	—	0.25–0.32	—	—	—
Drazen <i>et al.</i> (2008)	Plunger	1–2	3000–12 000	0.35–0.55	$3–9 \times 10^6$	Wave maker	Camera & wave gauges
Duncan <i>et al.</i> (1999)	Spiller	0.77	2105	0.31	2×10^6	Wave maker	Camera
—	Spiller	1.18	5000	0.31	4×10^6	—	—
Duncan (2001)	Spiller	0.41	600	0.275	8×10^5	Wave maker	Camera
Liu & Duncan (2003, 2006)	Spiller	0.4–0.65	1000–1750	0.317	$8–16 \times 10^5$	Wave maker	Camera
Fedorov <i>et al.</i> (1998)	PCW	0.1	35	0.28, 0.29, 0.33	10×10^4	Wave maker	Wave gauges
—	PCW	0.07	15	0.2, 0.22, 0.25	5.8×10^4	—	—
—	PCW	0.05	8	0.11, 0.16, 0.2	3.5×10^4	—	—
Caulliez (2013)	Spiller	0.12, 0.17	50, 100	0.34, 0.37	$13, 22 \times 10^4$	Wind	Camera
—	PCW	0.05–0.12	9–50	0.26–0.42	$3.5, 13 \times 10^4$	—	—
—	Plunger	0.25	215	0.5	39×10^4	—	—
Zhang (1995)	PCW	0.075, 0.05	19, 9	0.21, 0.25	$3.5, 6 \times 10^4$	Wind	Camera
Perlin <i>et al.</i> (1993)	PCW	0.068, 0.105	16, 38	0.22, 0.24	$3.5, 10 \times 10^4$	Wave maker	Camera
Jiang <i>et al.</i> (1999)	PCW	0.101	35	0.11–0.25	10×10^4	Wave maker	Camera
—	PCW	0.073	18	0.08–0.22	6×10^4	—	—
—	PCW	0.066	15	0.1–0.21	5×10^4	—	—
—	PCW	0.05	8.6	0.03–0.15	3.5×10^4	—	—
—	PCW	0.045	7	0.13–0.16	3×10^4	—	—
Banner & Peirson (2007)	Breakers (MI)	0.38–0.46 m	500–766	0.11–0.17	$3–9 \times 10^6$	Wave maker	Wave gauges
Tulin & Waseda (1999)	Breakers (MI)	0.4–4	500–50 000	0.1–0.3	$0.8–20 \times 10^6$	Wave maker	Wave gauges

Figure 15: Experimental parameters of observed parasitic capillary waves, spilling and plunging breakers available from the literature. Adapted from [40].

3.1.1. Breaking onset

Recently a new criterion for the breaking onset, has been proposed by Professor Banner and co-workers [35]. This criterion suggests that the onset of breaking occurs when the wave crest celerity displays a deceleration. At the recent B’Waves 2016 symposium, Professor Banner invited us to check whether our data displayed a wave crest slowdown at the verge of breaking.

Because the relatively large time step used in the PIV analysis (i.e. $dt =$

1/16s) does not allow a time-resolved estimation of the wave crest speed, we have used the images from a digital camera with 25 fps and spatial resolution $1920 \times 1088px$ to evaluate the wave crest slowdown. Hence, from the available images we measured the horizontal wave crest position, as shown in Fig. 16 (left panel), where the dashed line represents the average value of the horizontal position of the wave crest determined through 7 repetitions of the same run; the corresponding standard deviation is represented by the errorbar. Because the measurement was done manually, an under sampling technique was used to reduce the effort; this means a temporal resolution of 8 fps, i.e. a time step of 0.125s. This preliminary analysis enables an estimation of the wave crest celerity, whose results are reported, in a dimensionless fashion, in the right panel of figure 16; the minimum crest celerity occurs around $t^* = 13$.

To improve the analysis we increased the time resolution (frame by frame) in a window around $t^* = 13$ and including the time when we first observed some air trapping (here taken as a rough estimate for wave breaking inception). The videos of two different runs were analysed and the results are shown in the left panel of Fig. 17 by means of the green and blue symbols. Such measurement is within the errorbar of the previous one obtained as the mean of 7 runs, testifying the repeatability of the phenomenon. The dimensionless horizontal component of the velocity of the wave crest, reported in the right panel of Fig. 16 (green and blue symbols), displays significant deviations from the red line. In particular, its minimum corresponds to the instant $t^* = 12.046$, which, according to Barthelemy et al. [35] represents the onset of breaking. The same authors suggest that the breaking onset occurs when the air trapping starts at a significantly lower initial velocity than expected. The images of Fig. 17, seem to support such observation: the first image, at $t^* = 11.77$, shows the free-surface configuration just before the air trapping inception; $t^* = 12.046$ is the time when air is first trapped and coincides with the time of minimum crest celerity.

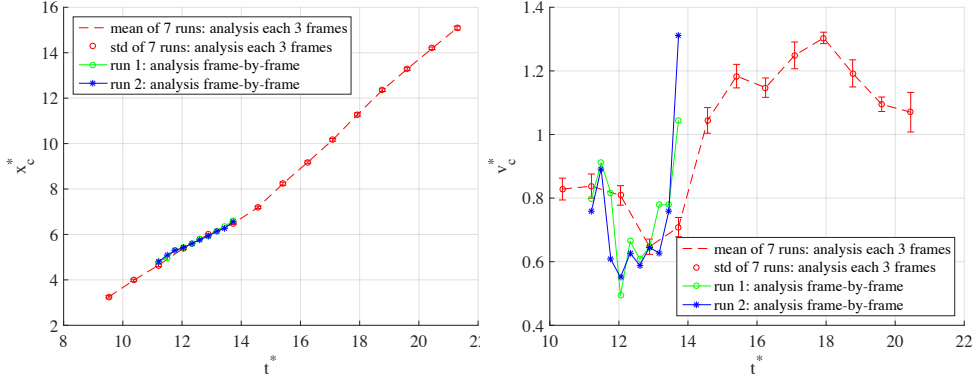


Figure 16: Evolution of the wave crest displacement (left panel). Velocity of the wave crest (right panel).

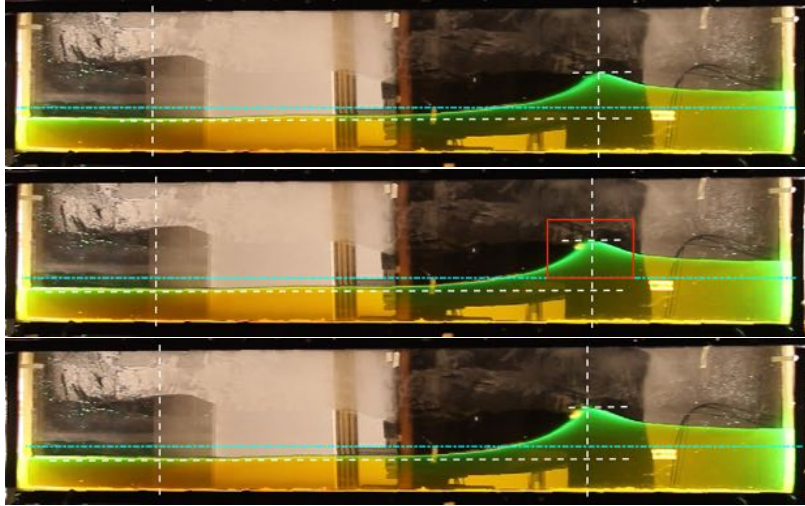


Figure 17: Visual observation of the wave crest evolution at times, from top to bottom, $t^* = 11.766, 12.046, 12.326$.

3.1.2. Mean velocity field

The mean and turbulent flow components were obtained through an ensemble-average of the instantaneous velocity. The mean velocity was calculated as

$$\langle \mathbf{v} \rangle = \frac{\sum_{i=1}^N \mathbf{v}}{N} \quad (4)$$

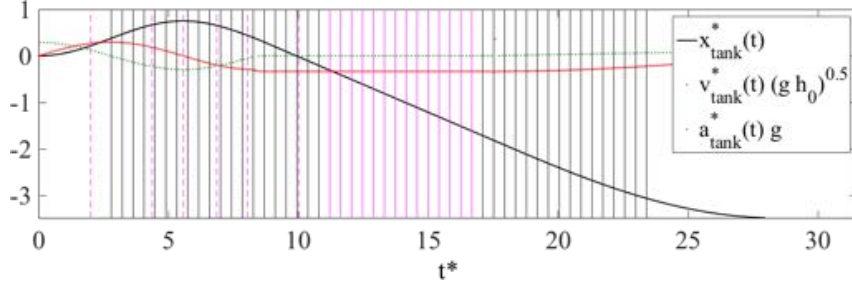


Figure 18: Time history of the motion (black bold line), velocity (dotted red line) and acceleration (dotted green line) of the tank. The continuous lines correspond to the times of the images of interest.

where $\mathbf{v} = (u, v)$ are the components of the instantaneous velocity in the (X, Y) coordinate system and $\langle \mathbf{v} \rangle = (U, V)$ are the related mean components.

The turbulent velocity components were evaluated as:

$$\mathbf{v}' = \mathbf{v} - \langle \mathbf{v} \rangle \quad (5)$$

For a proper understanding of the kinematic field in the wave body, we refer to the prescribed motion of the tank, which is shown in Fig. 18 with the black bold lines, along with its velocity (dotted red line) and acceleration (dotted green line). In the same figure, the times corresponding to the experimental images are indicated by the continuous lines. Because the main focus of the present analysis is on the turbulent layer evolution, only the images between $t^* = 11.21$ and $t^* = 16.67$ (magenta continuous lines in Fig. 18) have been analysed. However, the initial evolution of the kinematic field is essential to fully understand the onset and the evolution of the breaking wave. Hence, we use the results of the HPC numerical solver; the chosen times are indicated by the magenta dashed lines in the tank motion history (see Fig. 18), while the corresponding images of the internal velocity field are shown in Fig 19.

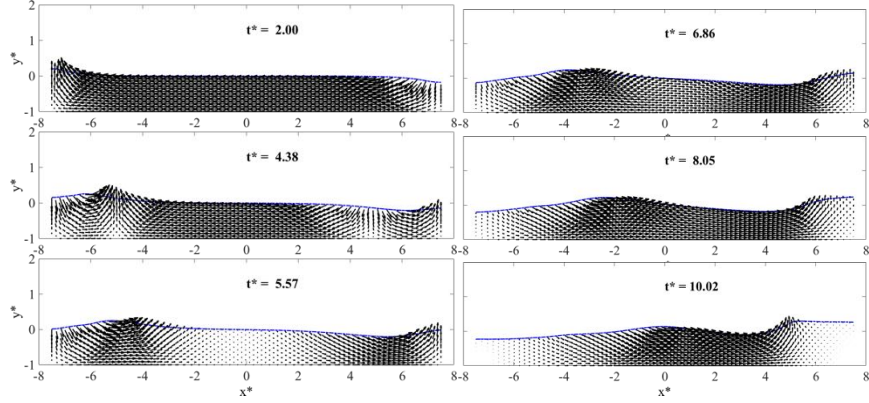


Figure 19: Image sequence of the velocity field evolution by the HPC solver.

At the beginning the tank is moved rightward, inducing a runup on the left wall and a rundown on the right side as a consequence of the standing wave connected with the highest sloshing natural period of the tank (see $t^* = 2$ in Fig. 19). Due to the impulsive start of the tank and to the shallow-water condition, higher modes are quickly excited. This is testified by the velocity field shown at $t^* = 4.38$ in Fig. 19, which highlights a convergent line on the left side ($x^* \approx -1$) and a divergent line on the right side (approximately at $x^* \approx 1$) of the tank, distinctive of the third sloshing mode. A rightward propagating wave is generated at $t^* = 5.57$, corresponding to the time of the reverse tank motion; such flow counteracts the wave generated at the right wall by the reverse motion of the tank and propagating leftward (see $t^* = 6.86 - 8.05$). The interaction between the reverse waves causes, first, a stagnation region at the right wall (see panel at $t^* = 10.02$ in Fig. 19) and, then, the onset breaking.

The following evolution of the mean velocity is shown on the left column of Figure 20, through the results of the experimental analysis. The related streamlines are also reported on the right column of the same figure. Because of the light saturation of the two-phase turbulent layer, such layer has been removed through a gray-scale filtering of the images. The dashed lines on each panel of the right column represent the upper boundary of the two-phase layer, while the continuous line provides the single-phase free-surface. At these instants,

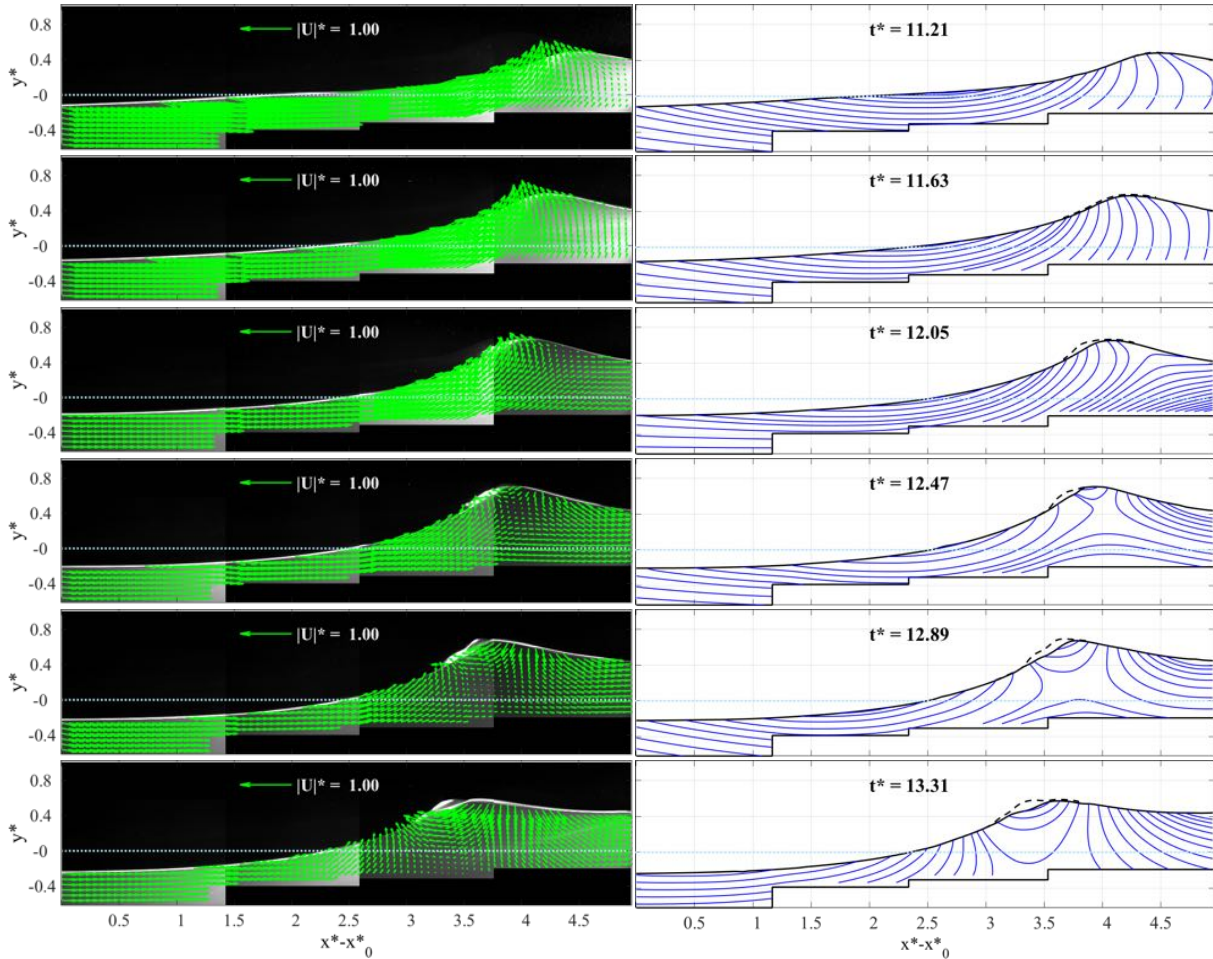


Figure 20: continue

corresponding to the magenta continuous lines of Fig. 18, the tank is moving leftward with a uniform motion. A first visual inspection of the velocity field, shows that the tank motion, along with the interaction of the two reverse waves, causes an upward flow with a steepening of the free surface from $t^* = 11.21$ (top panels of fig. 20) to $t^* = 12.47$ (fourth row of the same figure).

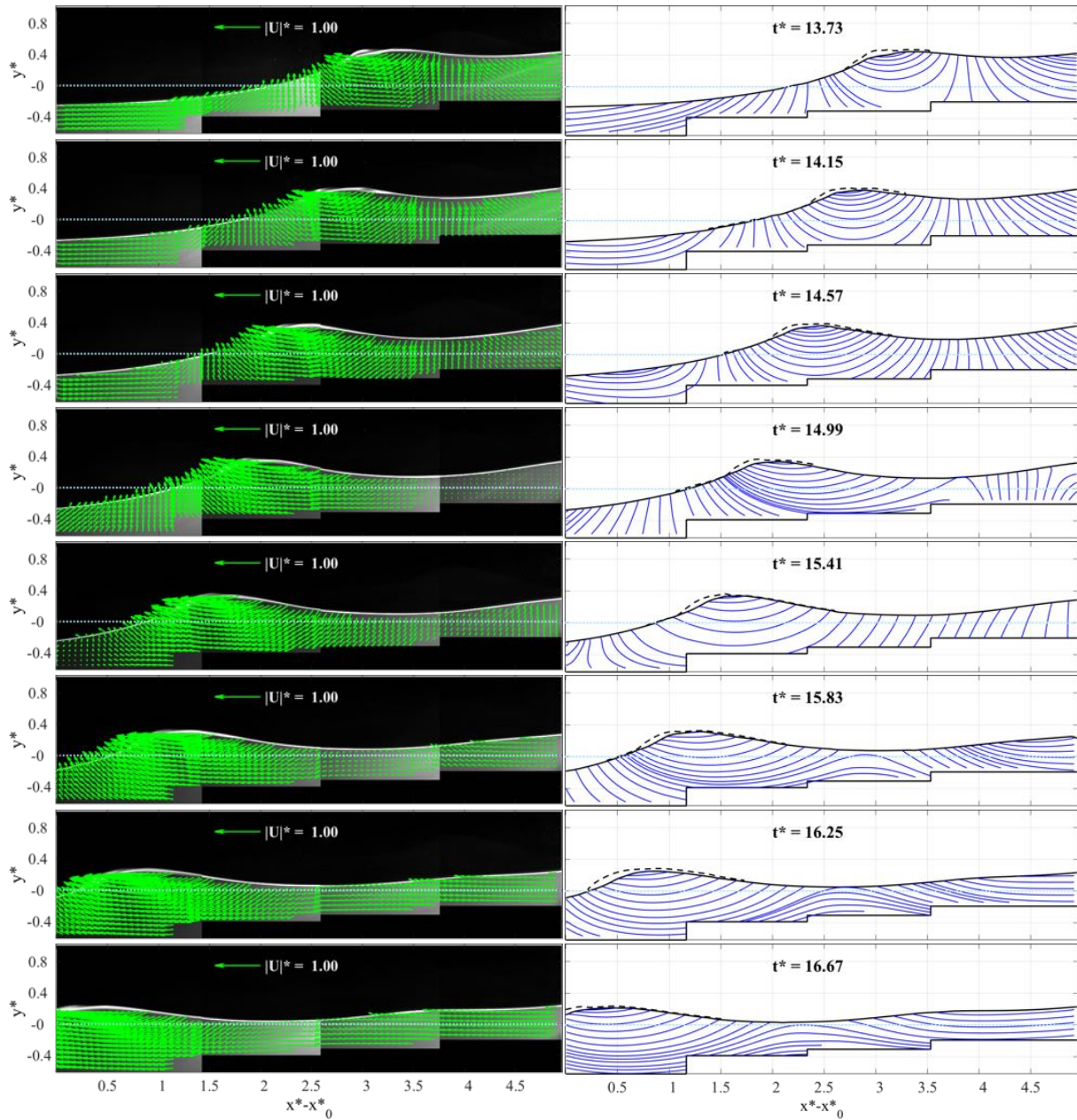


Figure 21: Image sequence of the evolution of the internal mean velocity field.

However, the reverse flow interaction of the two waves governs the onset and the kinematics of the breaking wave, with a portion of the leftward wave which rides on top of an underlying “return flow” from the rightward propagating wave, this leading to an oblique divergent flow (see $t^* = 12.05$ of Fig. 20). In more detail, for $11.21 \leq t^* \leq 12.05$, the flow just at the lee and below the crest of the wave is largely upward, fed by the incoming opposite waves, and induces a slowdown and steepening of the wave crest. Then breaking occurs (i.e. $t^* = 12.05$, see the previous section) and at $t^* = 12.47$, the still active wave interaction originates the splitting of the flow in four rotating flow regions: i) a lower flux moving clockwise and ii) an upward counterclockwise flow, both consequence of the wave propagating from left to right, iii) a downward counterclockwise and iv) an upper clockwise flow regions as consequence of the wave generated at the right wall and moving leftwards. These regions originate two flow lines, convergent and divergent, respectively (see Fig. 22), intersecting one another and generating a quadrupolar structure with a central saddle point. Very similar structures have been observed in numerical calculations of spiller and plungers ([42]).

The mentioned structure evolves towards the front of the wave, its center deepening of about $0.2h_0$ below the crest at $t^* = 12.47$ and of about $0.4h_0$ below the aerated breaker surface at $t^* = 12.89$. Over this period the wave steepness ($kH/2$) increases to reach its maximum of 0.25 at $t^* = 12.89$. It, thus, seems that the energy-based breaking occurs sometime before the largest wave height ($12.47 \leq t^* \leq 12.89$, see Fig. 14) and steepness (see also Fig. 14) are reached, such lags providing some measure of the wave inertia in its shoaling and steepening processes.

The mentioned flow structure, moves downward and in both the horizontal directions (see $t^* = 12.89$ of Fig. 20). In particular, it presses down region i), squeezing it, from $t^* = 12.89$ to $t^* = 14.15$, to the tank bottom. The consequent weakening of the quadrupole induces a flattening of the free-surface after $t^* = 14.57$, which preludes to the evolution of a quasi-steady breaker. In this second stage of evolution, the following main dynamics: evolve the near-

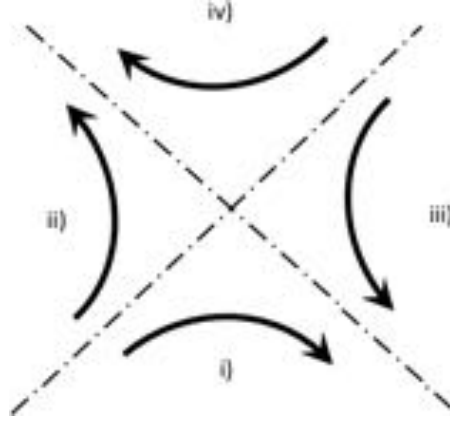


Figure 22: Sketch of the saddle-point at a quadrupole.

surface flow of the breaker, part of the upper portion of a quadrupole and moves in the direction of the crest motion; the quadrupole deepens and weakens, its center moving towards the bottom of the tank and the front of the wave; the wave slowly flattens preludeing to a quasi-steady evolution, as a consequence of the slow weakening of the quadrupolar structure.

3.1.3. The vorticity

Notwithstanding the evolution of the flow structures described in the previous section, a detailed analysis of the mean vorticity (i.e. associated with the mean flow) reveals that the body of the wave is almost irrotational, the vorticity being confined to the near-surface region (see Fig. 24). The flow related with the two-phase flow region has been removed by applying a gray scale filtering of the images. At the first instant that we consider useful for the analysis, $t^* = 11.21$, a layer of counterclockwise (positive) vortical flow is evident far upstream of the wave crest, the lee side of the crest being characterized by some very small counterclockwise vorticity. At $t^* = 11.63$ much stronger vorticity ($20 \leq \omega^* = \omega\sqrt{h_0/g} \leq 25$) is observed exactly at the wave crest and using a vorticity-injection-based criterion this would be the time of breaking inception. However, in view of the fairly coarse temporal resolution available ($\Delta t^* = 0.42$),

it is possible that the actual vorticity-based breaking onset occurs in the interval $11.21 \leq t^* \leq 11.63$. These times suggest that the vorticity-based onset slightly anticipates the energy-based breaking onset time, $t^* = 12.046$, given by the energy criterion illustrated in the previous section.

At later times the vortical layer lengthens down the front face of the wave, increases in intensity and thickness (because of diffusion), till time $t^* = 12.89$ when the maximum wave steepness is reached and the peak of positive vorticity is well ahead of the wave crest. At the same time the crest deforms to assume a non-monotonic shape, made of two bumps, (i) crest and (ii) location of maximum vorticity upstream of the crest, and a small intermediate dip. The vorticity peak is just upstream of the free surface bump (ii) which, in turn, stays ahead of the crest (i) of a fairly constant distance (about $h_0/2$) till the end of the observation ($t^* = 16.25$) and, in view of the common knowledge on wave breaking, might be regarded as the toe of the breaker. One notable feature evolving from $t^* = 13.73$ is the pulsation in intensity of the vorticity patch, which seems to alternatively undergo some weakening ($t^* = 14.14, 14.57, 16.25$) and strengthening ($t^* = 14.99, 15.41, 15.83$).

From what above, the mechanism of generation of vorticity seems more connected to the local deformations of the free-surface (i.e. increase of its curvature) rather than to the global steepening of the wave crest.

3.1.4. *The Turbulent Kinetic Energy*

The temporal evolution of the specific (per unit mass) Turbulent Kinetic Energy (TKE) (see Fig. 26), highlights the generation of an intense shear layer formed below the free surface of a fully-formed unsteady spilling breaker.

A small fraction of the maximum TKE (5%), has been chosen as the threshold to define the lower spatial boundary (pink dashed line) of the turbulent region, which in the analytical model, see section 1 and Fig. 1, gives $\Upsilon(t)$. The TKE is here made dimensionless with the velocity scale $\sqrt{gh_0}$, i.e. $TKE^* = TKE/\sqrt{gh_0}$. The upper boundary of the thin single-phase turbulent layer, instead, has been determined through gray scale filtering of images and excludes

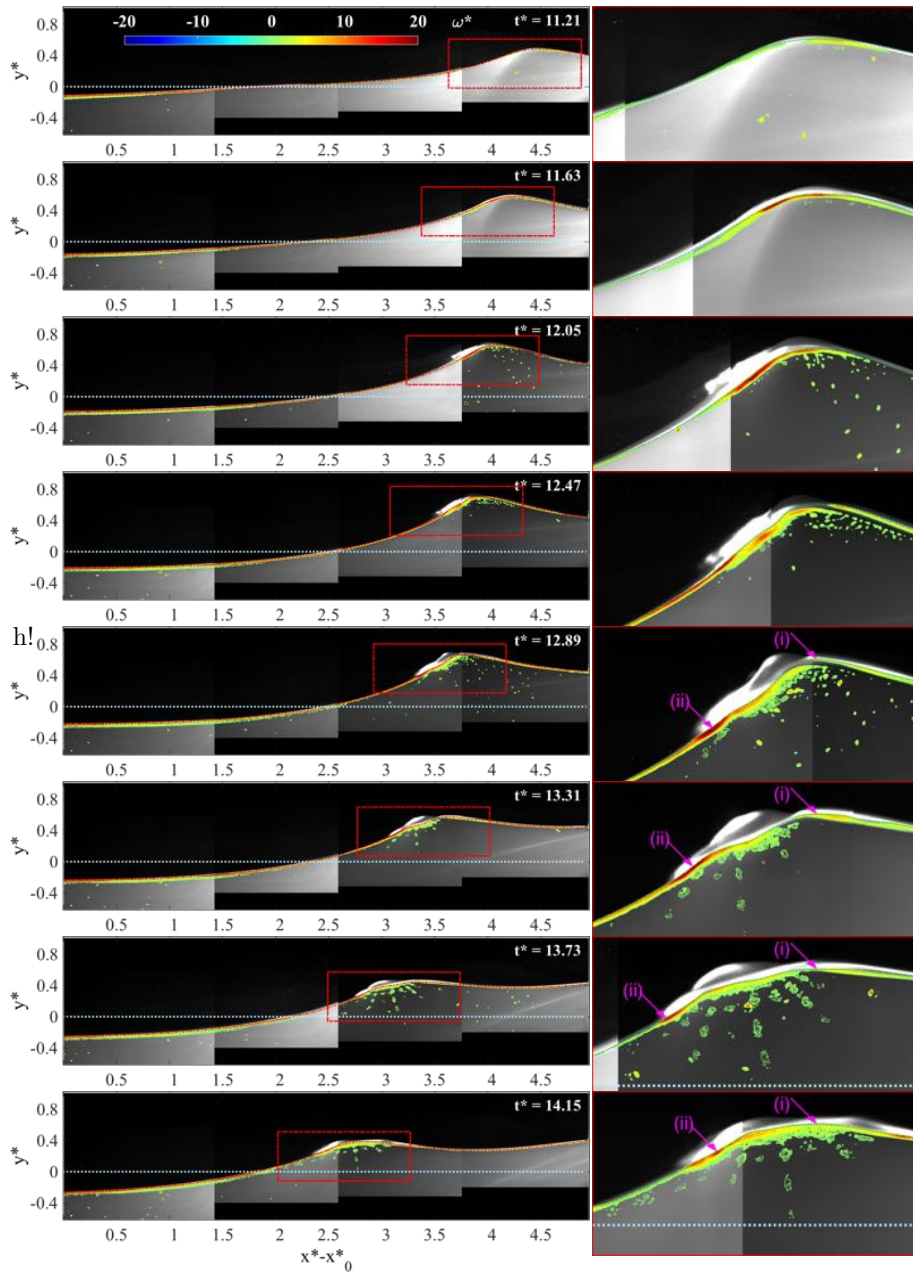


Figure 23: continue

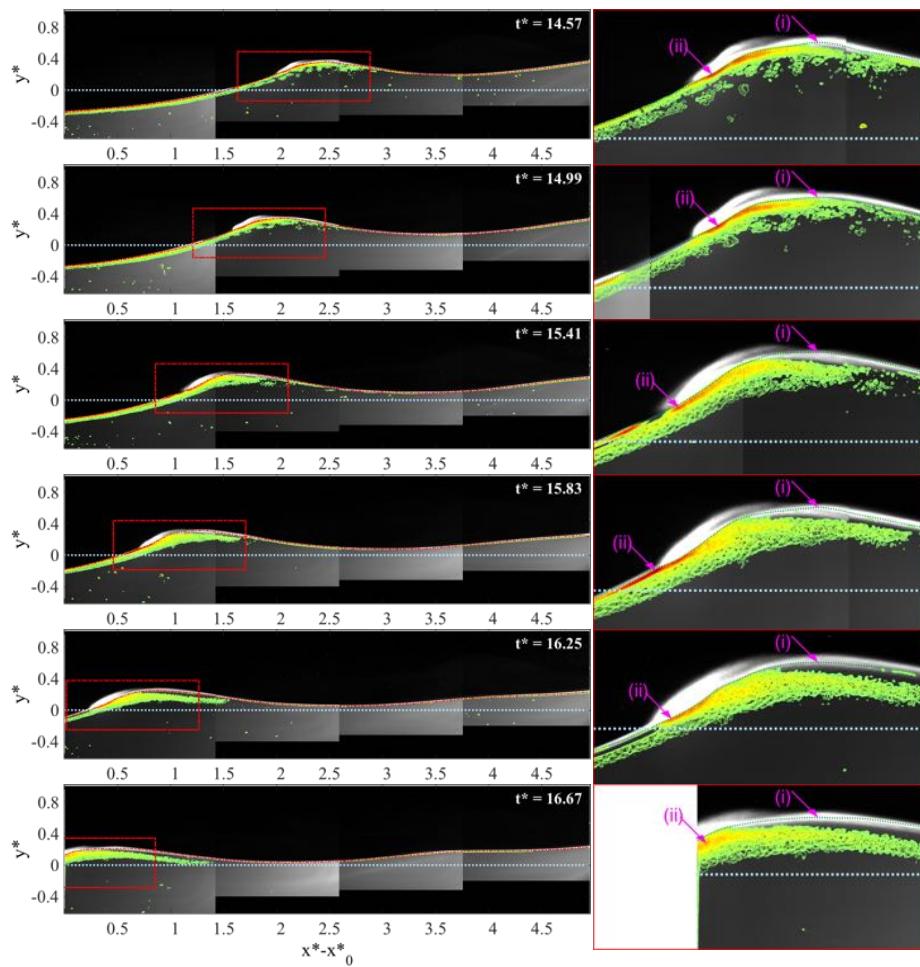


Figure 24: Image sequence of the generation and evolution of the vorticity in the shear layer for an unsteady spilling breaker.

the two-phase turbulent layer.

The spatial and temporal evolution of the TKE (shown in Fig. 26) have been analyzed from $t^* = 11.21$. However, it is only at time $t^* = 11.63$ that some intense turbulence is visible at the front face of the wave, slightly downward, more upstream (about $h_0/3$) of the peak of vorticity (generation of TKE, labelled as “phase a”). This instant exactly coincides with the vorticity-based onset of breaking and almost exactly with the onset predicted through the energy-based criterion (at time 12.046, see previous section). Like for the vorticity, the patch of TKE is seen to slide and lengthen down the front face of the wave, its peak ($TKE^* \sim 0.020 - 0.025$) being still more upstream than the peak of vorticity and reaching the toe of the breaker at $t^* = 13.31$ (downward slide of turbulence, labelled as “phase b”). Also, similarly to the vorticity, the TKE peak is placed below the more upstream of the two local bumps visible at the wave crest (i.e. bump (ii)). All the events here described evolve during stage (1) of evolution of the TKE. Such coherent stage of evolution is also reflected in the analysis of the geometry of the turbulent layer (see the subsequent section).

Later, during stage (2), which begins at $t^* \geq 13.73$, similarly to the vorticity, the TKE, though steadily diffusing in the lower region of the flow, is characterized by an intensity pulsation made of sudden decays ($t^* = 13.73, 14.15, 16.25$) and growths ($t^* = 14.57, 14.99, 15.41$) of its peak values. Moreover, the region over which the TKE diffuses is slightly smaller than that over which the vorticity diffuses. We believe that the above effects, pulsation and reduced diffusion, are due to some centrifugal action related with the curvature and local rotation of the single-phase turbulent layer, here measured with κ and Ω , respectively. These aspects will be analysed in detail in a dedicated work.

In other words, the gradual decrease of wave steepness, which occurs for $t^* = 13.73$ is accompanied by unsteady local effects related with the pulsation of the local flow curvature, rotation and thickness of the turbulent layer. Hence, like for the vorticity, also the TKE seems to be more significantly affected by local rather than global dynamics.

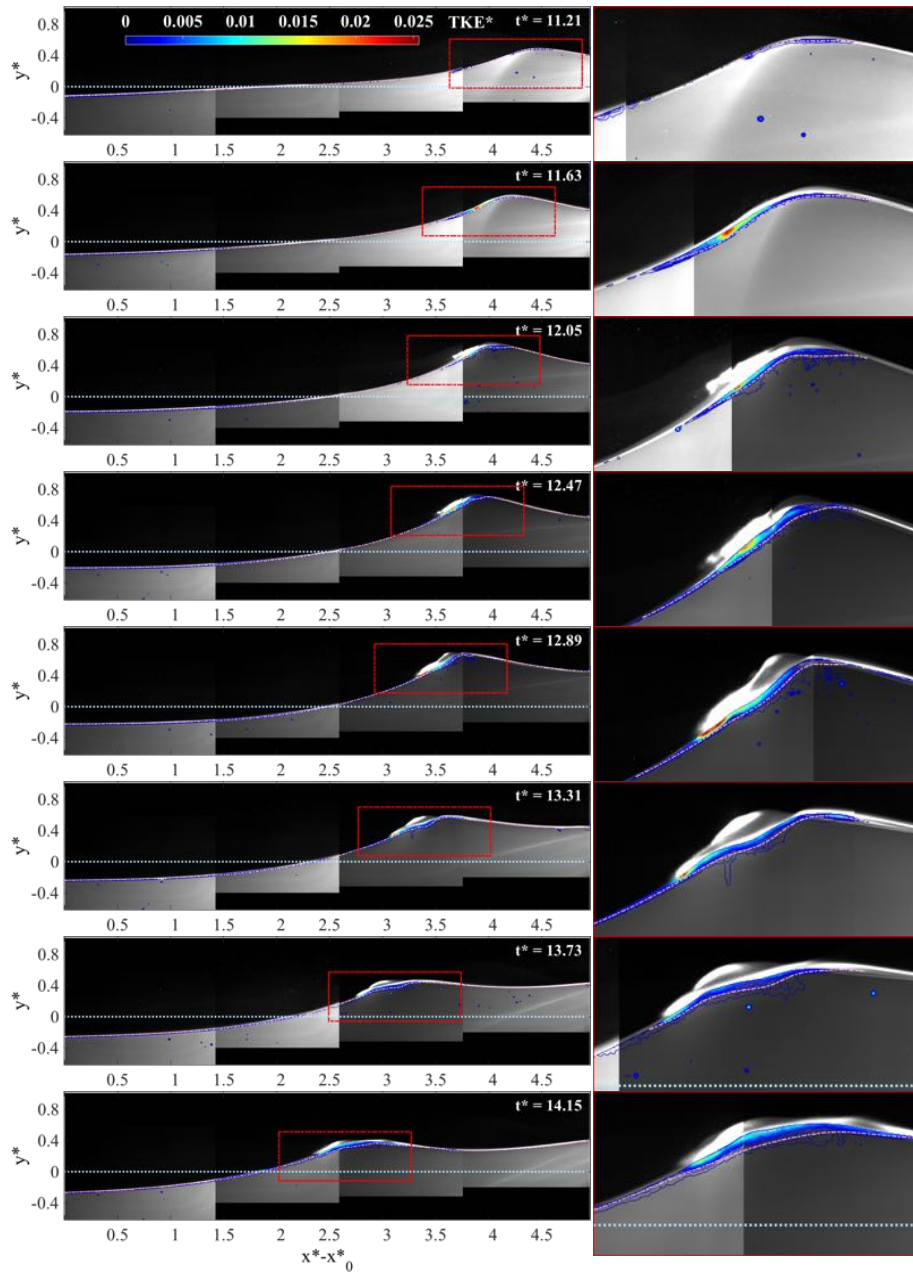


Figure 25: continue

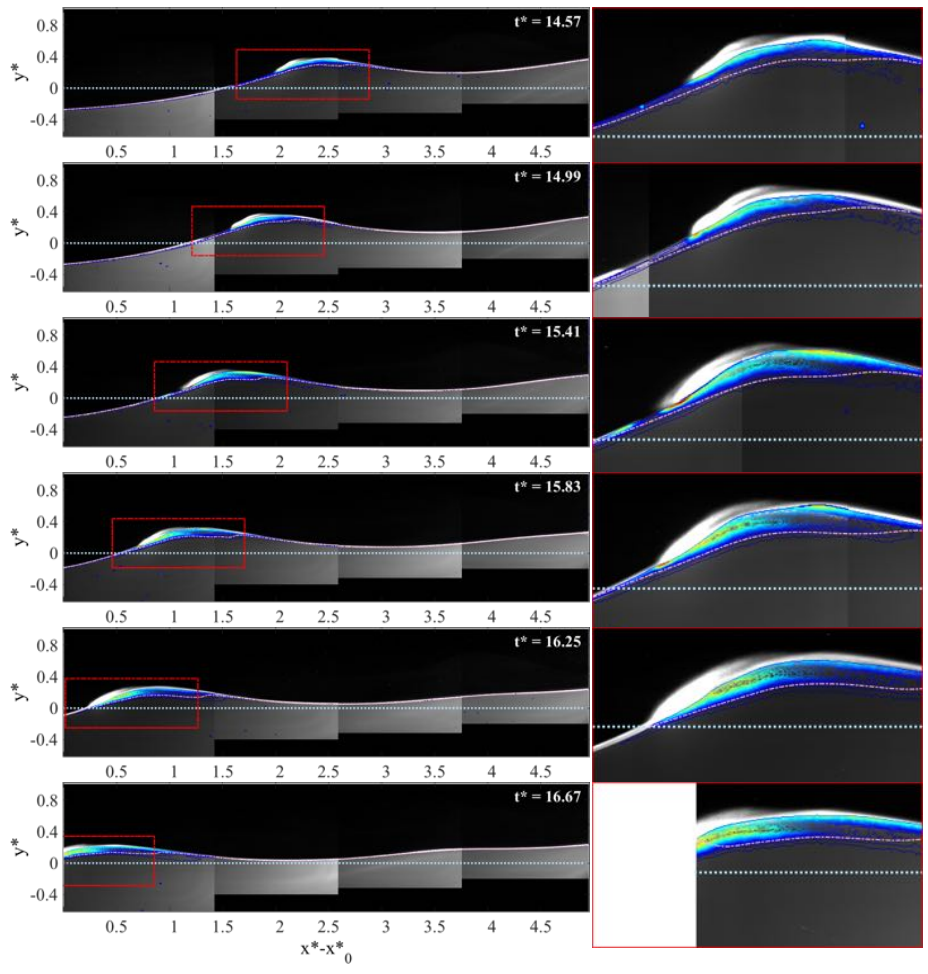


Figure 26: Image sequence of the generation and evolution of the TKE in the shear layer of an unsteady spilling breaker.

During the final stages of interest ($t^* \geq 16.25$) the Υ interface becomes almost parallel to the tank bottom with the turbulent region closely resembling that evolving into a quasi-steady hydraulic jump.

3.2. Geometry of the single-phase turbulent region

In this section, the attention is focused on the geometric characteristics (thickness (b), streamwise length (L_s) and relative thickness ($\epsilon = b/L_s$)) of the single-phase turbulent layer, as described in the theoretical model by Brocchini [18] (see Fig. 27).

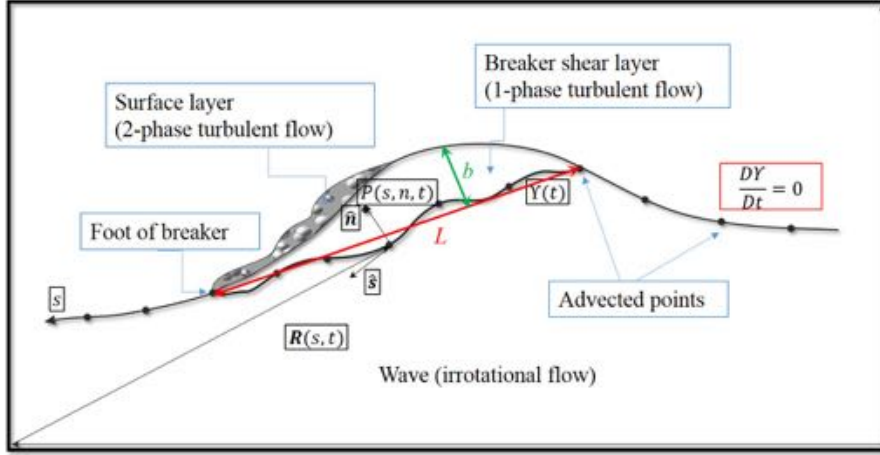


Figure 27: Schematic view of the theoretical model of Brocchini [18]

The analysis is similar to that of Misra et al. [24], who used their experimental data for a hydraulic jump (steady phenomenon) to provide estimates of the geometry of the shear layer as a proxy for the single-phase turbulent region of a spilling breaker.

In that case, the shear layer, being caused by a quasi-steady hydraulic jump, was characterized by one single value of ϵ , independent of time. On the opposite, our unsteady breaker is characterized by thicknesses and length that are functions of time and also of the position downstream of the breaker toe.

Fig. 29 illustrates the evolution in time of the single-phase layer thickness (b) and length (L_s). Such thickness has been evaluated through the intersection

of the limit curves that defines the shear layer. The red dashed line visible in each plot, represents the maximum possible experimental error (2 px/mm). The first point, located at zero abscissa, is at the toe of the breaker, here taken as the most upstream point of the single-phase turbulent region.

Two main stages of evolution are here visible. Stage (1), goes from $t^* = 11.63$ to $t^* = 13.73$ and it is characterized by an almost constant maximum thickness of about 0.03 and length pulsation around the value of 1. This first stage includes both phases of (a) generation of TKE and (b) downward slide and lengthening of the single-phase turbulent region, described in the previous section.

The second stage, (2), begins at $t^* = 14.15$ when the layer thickness rapidly and unsteadily increases from 0.05 to the maximum value of about 0.1 at time $t^* = 15.41$, settling to about the same value for longer times. During the same stage the length of the single-phase turbulent region oscillates between 1.5 and 2. These behaviors are well evident in Figs 30 and ??, which, respectively, give the evolution in time of the maximum layer thickness and length. The blue circles and the dashed line give, respectively, the effective measures of the maximum shear layer thickness and the interpolating polynomial, fourth-order for b and third-order for L_s . Hence, this second stage coincides with the vorticity and TKE pulsation stage described in the previous sections.

The above clear subdivision seems to occur at the time when the crest steepness significantly decreases and the pulsation in thickness observed during the second stage seems to be related with the pulsation of local curvature and rotation of the turbulent layer.

Attempting at a comparison with the literature, we find that in Misra et al. [24], the dimensionless streamwise variation of the width of the layer, increased linearly until 0.29, after which it becomes constant and the flow resembles a wake. In any case, the thickness of the turbulent region observed by Misra et al. [24] is very large compared with our results.

Finally, the thickness parameter ϵ , is shown in Fig. 31. Also this function has been interpolated with a fourth-order polynomial, like b . The maximum value achieved is about 0.06, which is the same of that observed by [43] for

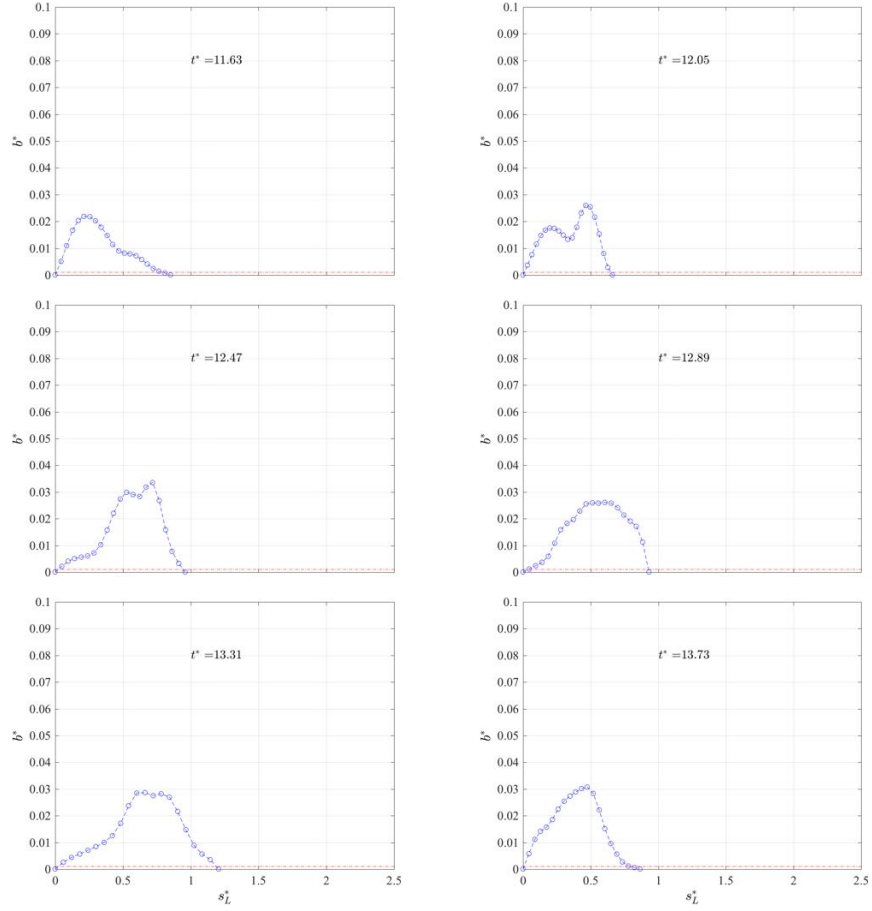


Figure 28: continue

jets and mixing layers (values of order 0.06). In Misra et al. [24], values of ϵ averaged over the breaker shear layer were of the order 0.03, which is slightly smaller compared with our results and those of Tennekes and Lumley [43]. These values are small enough to justify use of the “thin layer” approximation.

Fig. 31 also highlights the clear separation of stages (1) and (2), this occurring around $t^* = 14.15$.

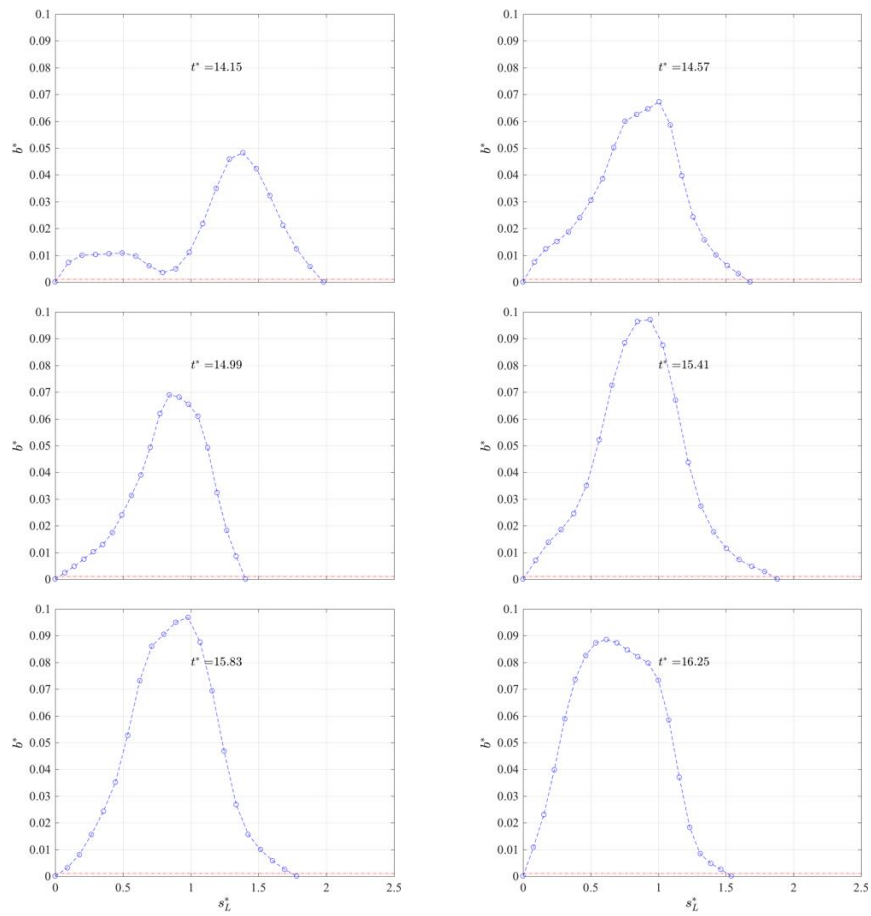


Figure 29: Evolution in time of the single-phase layer thickness plotted against normalised curvilinear abscissa: the time is increasing from left to right, from top to bottom.

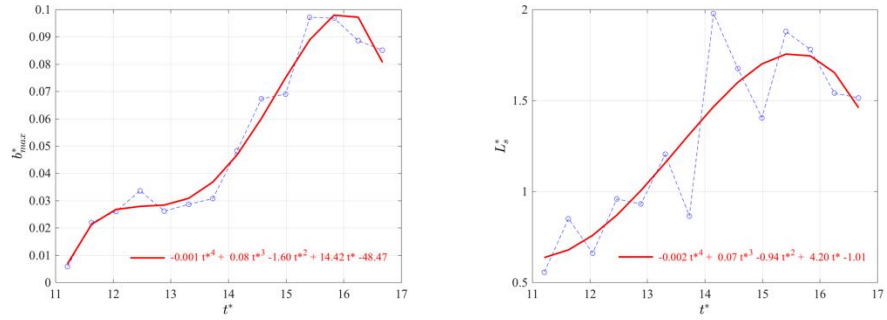


Figure 30: Time evolution of the maximum thickness of the single-phase layer (left panel) and of the interface length (right panel).

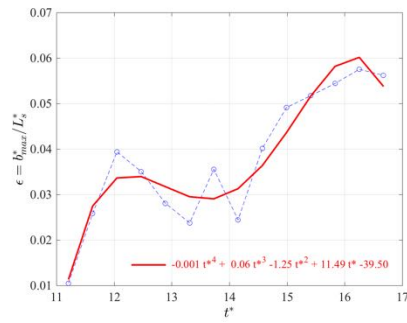


Figure 31: Evolution of thickness parameter in time.

4. Mean velocity profile in the shear layer

One first contribution of the present preliminary analysis to the evaluation of the model of Brocchini and co-workers relates to the analysis of the mean field within the single-phase turbulent region. Following the idea of Madsen and Svendsen [44], a cubic polynomial profile was used by Brocchini and co-workers for the cross-flow profiles. In this way it is possible to get a quantitative description of the flow by means of the simplest profile that allows for an inflection point.

Assuming a vanishing shear stresses at the interface with the irrotational flow underneath and the continuity of the mean velocity at the top and bottom of the single-phase turbulent layer, the mean streamwise velocity, is equal to:

$$U(s, \sigma, t) = \hat{U} + (U_b + \hat{U}) \sigma^2 + A [U_b - \hat{U} - b(s, t)\Omega] \sigma^2 (1 - \sigma) \quad (6)$$

where $\sigma = n/b(s, t)$, \hat{U} and U_b are, respectively, the mean streamwise velocities at the the bottom and top of the single-phase turbulent layer. For vanishing rotation $\Omega = 0$, the mean flow profile is:

$$U(s, \sigma, t) = \hat{U} + (U_b + \hat{U}) \sigma^2 + A [U_b - \hat{U}] \sigma^2 (1 - \sigma) \quad (7)$$

Using our experimental data, we can verify the ability of the analytical solution (7, selected times only, for brevity) to describe the mean velocity profile (Fig. 32). Assuming that in the local frame of reference it is $\hat{U} = 0$, a cubic polynomial (continuous magenta line) has been fit to the measured value of $U(s, \sigma, t)$. All the streamwise locations were analysed and for each instant the value of the parameter A has been calculated and shown with the related errorbar in Fig. 32.

Misra et al. [45], used the same approach, but because of the small thickness of the shear layer near the toe, few data points were available for a robust fit of the profile. Therefore, they chose the streamwise location in the middle part of the shear layer.

In the present case, diving (7) through U_b we get:

$$\frac{U(s, \sigma, t)}{U_b(s, t)} = \sigma^2 + A(s, t)(1 - \sigma)\sigma^2. \quad (8)$$

This enables us to retrieve the parameter $A = A(s, t)$, which weights the leading-order cubic term of (8) and it is an important parameter in the models of Brocchini and co-workers and of Madsen and Svendsen [44]. The observed behaviour is reasonable for the unsteady breaker we are analyzing and differs from Misra et al. [45], where their steady flow enabled computation of a time-independent parameter $A = A(s)$, seemingly comparable to the distribution observed at the onset of breaking, i.e. with A decreasing from the leading edge to the trailing edge of the turbulent layer.

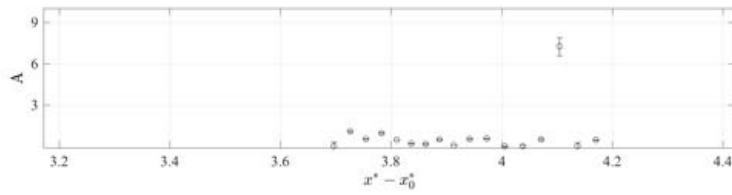
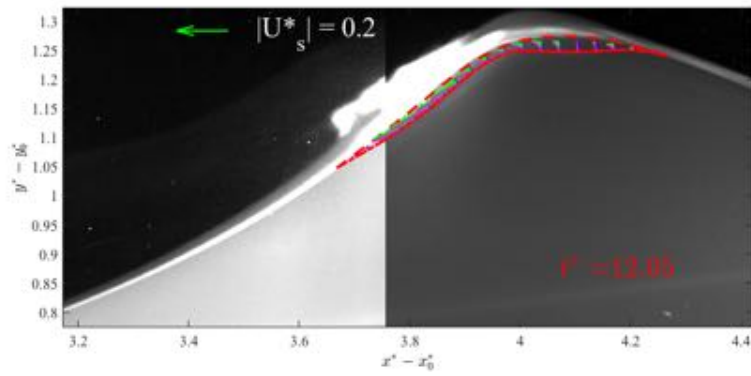
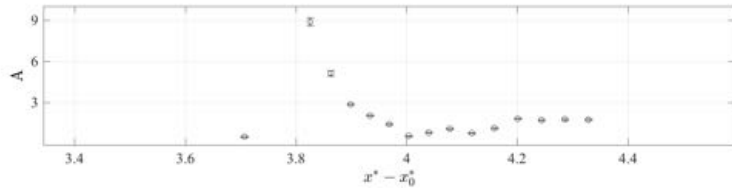
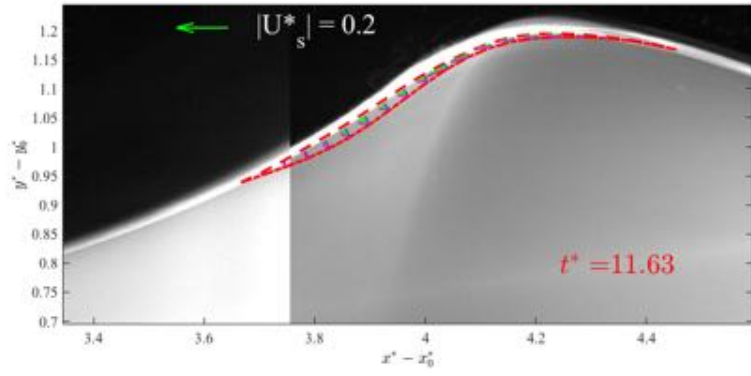
The evolution of the mean streamwise velocity profiles and of the behaviour of the parameter $A(s, t)$, matches the two-stage evolution above highlighted. During stage (1), which goes from $t^* = 11.63$ to $t^* = 13.73$, fairly small velocities are observed to occur within a fairly thin single-phase turbulent layer. After breaking the parameter $A(s, t)$ is characterized by fairly streamwise-uniform distributions with mean $A(s, t) = 1$. This means that, assuming $\Omega = 0$, the shear stress at the top boundary of the single-phase turbulent region is:

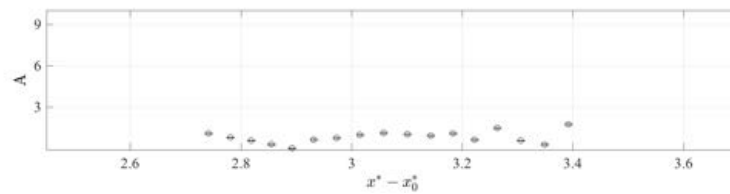
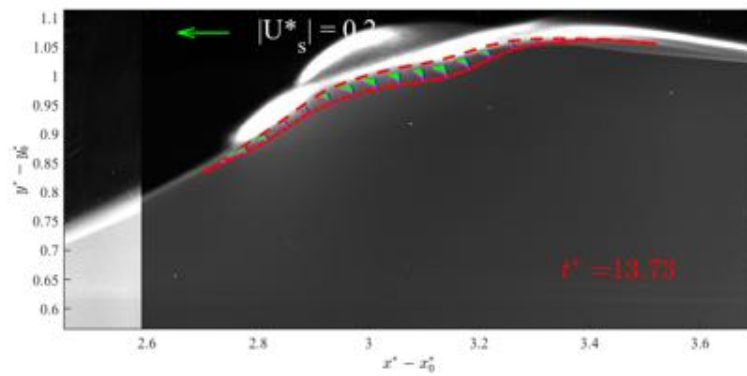
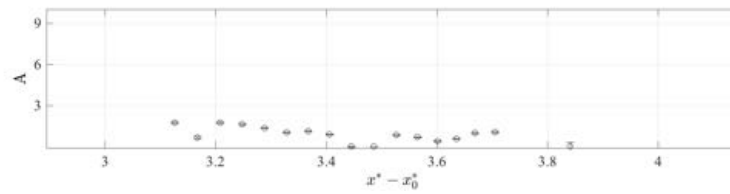
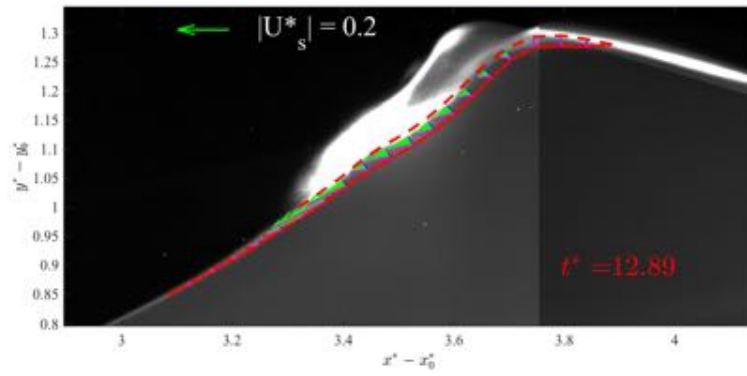
$$\frac{\partial U}{\partial n} \approx \frac{U_b}{b} > 0.$$

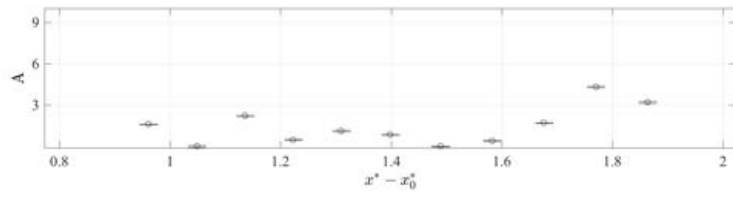
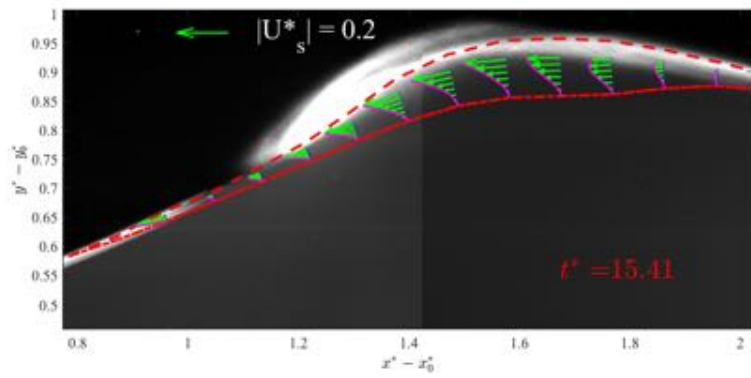
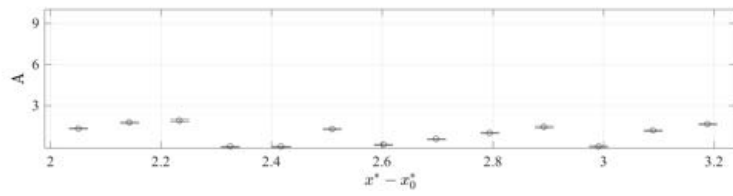
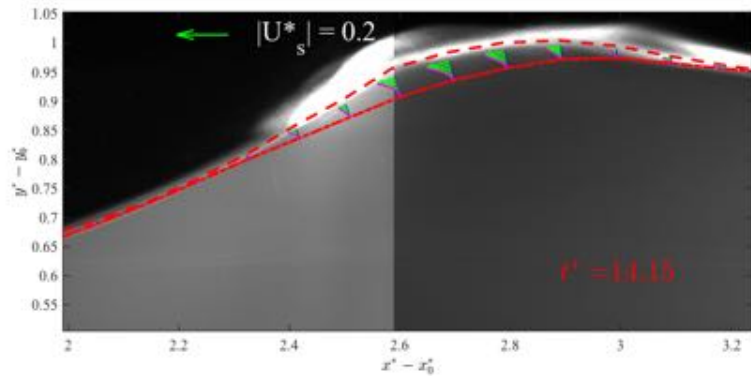
Noticeable is the very small size of the errorbar, testifying an excellent fit of the experimental data. On the other hand, stage (2), $14.15 \leq t^* \leq 16.25$, is characterized by significantly higher velocities over a much thicker single-phase turbulent layer and less streamwise-uniform distributions of $A(s, t)$. In particular, it is found that A increases from the leading edge of the turbulent region ($A \approx 1$) to its trailing edge, where A can become as large as 6 – 7. This means that, assuming $\Omega = 0$, the shear stress at the top boundary of the single-phase turbulent region is:

$$\frac{\partial U}{\partial n} \approx -C \frac{U_b}{b} < 0, \quad \text{with } C \sim 4 - 5.$$

This negative shear is clearly depicted by the velocity decreasing towards the top of the layer at the trailing edge of the turbulent region.







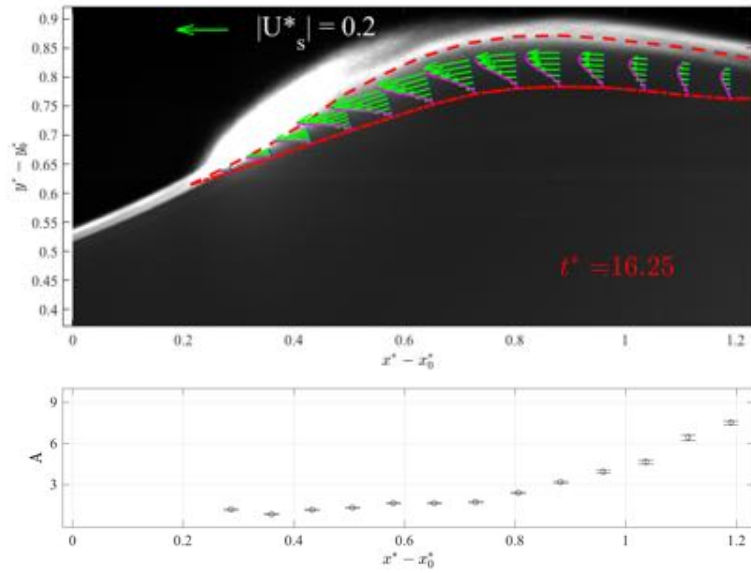
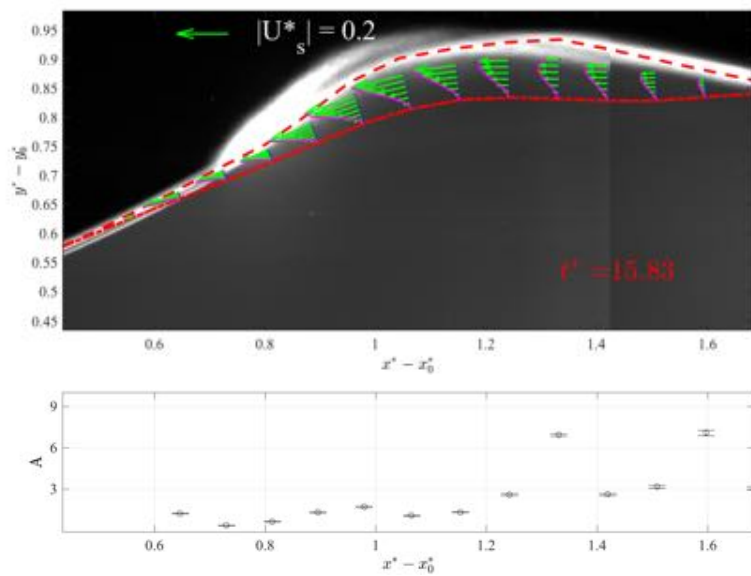


Figure 32: Evolution in time of the mean velocity profile in the thin single-phase turbulent layer.



5. Discussion and Conclusions

A twofold scope has been pursued by the present work, based on the analysis of accurate and reliable experimental data of a sloshing-induced, rapidly-evolving spilling breaker: 1) a detailed inspection and description of the overall flow evolution, 2) a specific analysis on the evolution of the near-surface, single-phase turbulence, also aimed at the validation of the theoretical model by Brocchini and co-workers.

The spilling in object has been obtained by the sloshing of a tank, whose motion has been accurately designed by using two different numerical solvers capable of reproducing the evolution of the wave both before (HPC solver) and after (NS solver) its breaking. Also the motion repeatability has been thoroughly checked and verified. The data at the basis of our analysis has been collected by means of PTV measurements of 2048 statistically-identical realizations.

The spiller is seen to evolve in shallow water, hence the use of scalings typical of shallow water flows (i.e. still-water depth h_0 for the lengths and $\sqrt{g/h_0}$ for the times). All results have been given in dimensionless form for portability.

The evolution of the breaker can be described in terms of both global and local features. Global characteristics, like wave height and wave steepness describe a flow characterized by an initial growth until the maxima of H and steepness are achieved at the times $t^* = 12.47$ and 12.89 after the start of the motion, respectively. However, while the wave height immediately and rapidly decays after peaking, the wave steepness remains constant at about 0.25 till $t^* = 14.15$ before decreasing.

The times of peaking of H and steepness are larger than the onset times for breaking based on various criteria. In summary, breaking is predicted to occur: at the earliest, $t^* = 11.63$, by the appearance of significant levels of both vorticity (at crest) and turbulence (slightly upstream of crest); slightly later by the energy-based criterion of Banner and co-workers (at $t^* = 12.05$), when also air entrainment is seen to start and somehow later by the attainment of maxima wave height and steepness.

The mean flow is characterized by a quadrupolar vortical structure connected by a saddle point, which at breaking onset is near the free surface at the lee of the crest. Later on the saddle point is seen to move upstream and downward of the wave crest. The mentioned flow structure has significant similarities with those observed in the numerical simulations by Watanabe et al [42]. However, a more detailed analysis is needed for a thorough comparison.

The most interesting dynamics are those related with the evolution of the vortical and turbulent flows. Two main stages characterize such evolution.

Stage (1) goes from the onset of breaking ($t^* = 11.63$) and includes the generation of vorticity and TKE (phase a) and their lengthening down the front face of the wave (phase b), till $t^* = 13.31 - 13.73$. At the end of this stage: a) the peaks of vorticity and TKE have reached their most upstream location, which can be regarded as the toe of the breaker, b) the whole crest has deformed, being it made of two bumps, one coinciding with the top of the crest (bump (i)) and one just downstream of the toe of the breaker (bump (ii)). During this stage the thickness and downstream length of the single-phase turbulent region remain almost constant ($b \approx 0.03, L_s \approx 1$). Fitting of the crossflow profiles of the mean streamwise velocities with cubic power laws is excellent and reveals a positive mean shear at the top of the layer.

Stage (2) goes from the peaks of vorticity and TKE reaching their most upstream location ($t^* = 13.31 - 13.73$) till the wave attains a quasi-steady shape ($t^* = 16.25$). This stage is characterized by a pulsation in intensity of both vorticity and TKE for which their peak values may increase/decrease of about 100%. This stage closes when the lower edge of the single-phase turbulent region Υ becomes almost horizontal and the wave undergoes a quasi-steady evolution. Fitting of the crossflow profiles of the mean streamwise velocities with cubic power laws suggests a negative mean shear at the top of the layer.

Because of the above, stage (1) can be regarded as “build-up” stage where vorticity and TKE rapidly grow to their maxima in intensity and extension, while stage (2) can be seen as a “relaxation” stage from the build-up to the following quasi-steady evolution, such a relaxation being characterized by some

significant flow pulsation. The analysis of the flow evolving over the above two stages suggests that vorticity and TKE are more influenced by local dynamics associated with the flow curvature and rotation than by global dynamics like the wave steepening, this is particularly visible during stage (1).

6. Acknowledgements

This work was partially supported by the Research Council of Norway through the Centres of Excellence funding scheme NTNU/AMOS, project number 223254.

References

- [1] G. B. Deane, M. D. Stokes, Scale dependence of bubble creation mechanisms in breaking waves, *Nature* 418 (6900) (2002) 839–844.
- [2] A. D. Clarke, S. R. Owens, J. Zhou, An ultrafine sea-salt flux from breaking waves: Implications for cloud condensation nuclei in the remote marine atmosphere, *Journal of Geophysical Research-Atmospheres* 111 (D6).
- [3] A. H. Callaghan, M. Stokes, G. Deane, The effect of water temperature on air entrainment, bubble plumes, and surface foam in a laboratory breaking-wave analog, *Journal of Geophysical Research-Oceans* 119 (11) (2014) 7463–7482.
- [4] E. Terray, M. Donelan, Y. Agrawal, W. M. Drennan, K. Kahma, A. J. Williams, P. Hwang, S. Kitaigorodskii, Estimates of kinetic energy dissipation under breaking waves, *Journal of Physical Oceanography* 26 (5) (1996) 792–807.
- [5] Z.-C. Huang, S.-C. Hsiao, H.-H. Hwung, K.-A. Chang, Turbulence and energy dissipations of surf-zone spilling breakers, *Coastal Engineering* 56 (7) (2009) 733–746.

- [6] A. Iafrati, Energy dissipation mechanisms in wave breaking processes: Spilling and highly aerated plunging breaking events, *Journal of Geophysical Research-Oceans* 116 (C7).
- [7] L. C. van Rijn, Prediction of dune erosion due to storms, *Coastal Engineering* 56 (4) (2009) 441–457.
- [8] C. Loureiro, Ó. Ferreira, J. A. G. Cooper, Extreme erosion on high-energy embayed beaches: influence of megarrips and storm grouping, *Geomorphology* 139 (2012) 155–171.
- [9] G. F. Clauss, Dramas of the sea: episodic waves and their impact on offshore structures, *Applied Ocean Research* 24 (3) (2002) 147–161.
- [10] M. Greco, M. Landrini, O. Faltinsen, Impact flows and loads on ship-deck structures, *Journal of Fluids and Structures* 19 (3) (2004) 251–275.
- [11] J. Duncan, Spilling breakers, *Annual Review of Fluid Mechanics* 33 (1) (2001) 519–547. [arXiv:http://dx.doi.org/10.1146/annurev.fluid.33.1.519](http://dx.doi.org/10.1146/annurev.fluid.33.1.519), doi:10.1146/annurev.fluid.33.1.519. URL <http://dx.doi.org/10.1146/annurev.fluid.33.1.519>
- [12] M. Perlin, W. Choi, Z. Tian, Breaking waves in deep and intermediate waters, *Annual Review of Fluid Mechanics* 45 (2013) 115–145.
- [13] F. C. Ting, J. T. Kirby, Dynamics of surf-zone turbulence in a spilling breaker, *Coastal Engineering* 27 (3) (1996) 131–160.
- [14] Y. Agrawal, E. Terray, M. Donelan, P. Hwang, A. J. Williams, W. M. Drennan, K. Kahma, S. Krtaigorodskii, Enhanced dissipation of kinetic energy beneath surface waves 359 (1992) 219–220.
- [15] D. H. Peregrine, *Mechanisms of Water-Wave Breaking*, Springer Berlin Heidelberg, Berlin, Heidelberg, 1992.
- [16] D. Peregrine, I. Svendsen, Spilling breakers, bores, and hydraulic jumps, *Coastal Engineering Proceedings* 1 (16).

URL <https://journals.tdl.org/icce/index.php/icce/article/view/3285>

- [17] M. L. Banner, , D. H. Peregrine, Wave breaking in deep water, *Annual Review of Fluid Mechanics* 25 (1) (1993) 373–397.
URL <http://dx.doi.org/10.1146/annurev.fl.25.010193.002105>
- [18] M. Brocchini, Flows with freely moving boundaries: the swash zone and turbulence at a free surface, Ph.D. thesis, University of Bristol, School of Mathematics. (1996).
- [19] M. Brocchini, D. Peregrine, The dynamics of strong turbulence at free surfaces. part 1. description, *Journal of Fluid Mechanics* 449 (2001) 225–254.
- [20] M. Brocchini, D. Peregrine, The dynamics of strong turbulence at free surfaces. part 2. free-surface boundary conditions, *Journal of Fluid Mechanics* 449 (2001) 255–290.
- [21] M. Brocchini, Free surface boundary conditions at a bubbly/weakly splashing air–water interface, *Physics of Fluids (1994-present)* 14 (6) (2002) 1834–1840.
- [22] S. K. Misra, J. T. Kirby, M. Brocchini, M. Thomas, F. Veron, C. Kambhamettu, Extra strain rates in spilling breaking waves, in: *Coastal Engineering Conference, Vol. 29, Asce American Society of Civil Engineers, 2004*, p. 370.
- [23] S. Gavriluk, V. Y. Liapidevskii, A. Chesnokov, Spilling breakers in shallow water: applications to favre waves and to the shoaling and breaking of solitary waves, *Journal of Fluid Mechanics* 808 (2016) 441–468.
- [24] S. Misra, J. Kirby, M. Brocchini, F. Veron, M. Thomas, C. Kambhamettu, The mean and turbulent flow structure of a weak hydraulic jump, *Physics of Fluids (1994-present)* 20 (3) (2008) 035106.

- [25] J. H. Duncan, A. A. Dimas, Surface ripples due to steady breaking waves, *Journal of Fluid Mechanics* 329 (1996) 309–339. doi:10.1017/S0022112096008932.
URL <https://www.cambridge.org/core/article/surface-ripples-due-to-steady-breaking-waves/05C701BBAE1349206A69CCDE70FE6BC9>
- [26] M. Antuono, A. Bardazzi, C. Lugni, M. Brocchini, A shallow-water sloshing model for wave breaking in rectangular tank, ”*Journal of Fluid Mechanics*”.
- [27] C. Lugni, A. Bardazzi, O. M. Faltinsen, G. Graziani, Hydroelastic slamming response in the evolution of a flip-through event during shallow-liquid sloshing, *Physics of Fluids* 26 (3). doi:http://dx.doi.org/10.1063/1.4868878.
URL <http://scitation.aip.org/content/aip/journal/pof2/26/3/10.1063/1.4868878>
- [28] A. Bardazzi, C. Lugni, M. Antuono, G. Graziani, O. M. Faltinsen, Generalized hpc method for the poisson equation, *Journal of Computational Physics* 299 (2015) 630–648. doi:10.1016/j.jcp.2015.07.026.
- [29] C. Lugni, M. Brocchini, O. M. Faltinsen, Wave impact loads: The role of the flip-through, *Physics of Fluids* 18 (12). doi:{10.1063/1.2399077}.
- [30] C. Lugni, M. Brocchini, O. M. Faltinsen, Evolution of the air cavity during a depressurized wave impact. II. The dynamic field, *Physics of Fluids* 22 (5). doi:{10.1063/1.3409491}.
- [31] C. Lugni, M. Miozzi, M. Brocchini, O. M. Faltinsen, Evolution of the air cavity during a depressurized wave impact. I. The kinematic flow field, *Physics of Fluids* 22 (5). doi:{10.1063/1.3407664}.
- [32] G. Colicchio, Violent disturbance and fragmentation of free surface, Ph.D. thesis, University of Southampton, School of engineering and the environment. (2004).

- [33] F. Scarano, Iterative image deformation methods in piv, *Measurement Science and Technology* 13 (1) (2002) 1–19.
URL <http://stacks.iop.org/0957-0233/13/i=1/a=201>
- [34] B. C. Abrahamsen, Sloshing induced tank-roof impact with entrapped air pocket, Ph.D. thesis, Norwegian University of Science and Technology, Trondheim, Norway. (2011).
- [35] X. Barthelemy, M. Banner, W. Peirson, F. Fedele, M. Allis, F. Dias, On the local properties of highly nonlinear unsteady gravity water waves. part 2. dynamics and onset of breaking, arXiv eprint arXiv:1508.06002.
- [36] A. Colagrossi, C. Lugni, M. Greco, O. Faltinsen, Experimental and numerical investigation of 2d sloshing with slamming, in: 19th International Workshop on Water Waves and Floating Bodies, Cartona, Italy, Mar, 2004, pp. 28–31.
- [37] B. Bouscasse, M. Antuono, A. Colagrossi, C. Lugni, Numerical and Experimental Investigation of Nonlinear Shallow Water Sloshing, *International Journal of Nonlinear Sciences and Numerical Simulation* 14 (2) (2013) 123–138. doi:{10.1515/ijnsns-2012-0100}.
- [38] O. M. Faltinsen, A. N. Timokha, Sloshing.
- [39] J. Williams, Limiting gravity waves in water of finite depth, *Philosophical Transactions of the Royal Society of London A: Mathematical, Physical and Engineering Sciences* 302 (1466) (1981) 139–188.
- [40] L. Deike, S. Popinet, W. K. Melville, Capillary effects on wave breaking, *Journal of Fluid Mechanics* 769 (2015) 541–569.
- [41] M. P. Tulin, T. Waseda, Laboratory observations of wave group evolution, including breaking effects, *Journal of Fluid Mechanics* 378 (1999) 197–232.
- [42] Y. Watanabe, H. Saeki, R. J. Hosking, Three-dimensional vortex structures under breaking waves, *Journal of Fluid Mechanics* 545 (2005) 291–328.

- [43] H. Tennekes, J. Lumley, A First Course in Turbulence, Pe Men Book Company, 1972.
URL <https://books.google.it/books?id=h4coCj-1N0cC>
- [44] P. A. Madsen, I. A. Svendsen, Turbulent bores and hydraulic jumps, Journal of Fluid Mechanics 129 (1983) 1–25. doi:10.1017/S0022112083000622.
URL http://journals.cambridge.org/article_S0022112083000622
- [45] S. K. Misra, M. Brocchini, J. T. Kirby, Turbulent interfacial boundary conditions for spilling breakers, in: Coastal Engineering Conference, Vol. 30, Asce American Society of Civil Engineers, 2006, p. 214.